

# Computer-Aided Detection and Diagnosis for prostate cancer based on mono and multi-parametric MRI: A review

Guillaume Lemaître<sup>a,c,\*</sup>, Robert Martí<sup>c</sup>, Jordi Freixenet<sup>c</sup>, Joan C. Vilanova<sup>d</sup>, Paul M. Walker<sup>b</sup>,  
Fabrice Meriaudeau<sup>a</sup>

<sup>a</sup>LE2I-UMR CNRS 6306, Université de Bourgogne, 12 rue de la Fonderie, 71200 Le Creusot, France

<sup>b</sup>LE2I-UMR CNRS 6306, Université de Bourgogne, Avenue Alain Savary, 21000 Dijon, France

<sup>c</sup>ViCOROB, Universitat de Girona, Campus Montilivi, Edifici P4, 17071 Girona, Spain

<sup>d</sup>Department of Magnetic Resonance, Clínica Girona, Lorenzana 36, 17002 Girona, Spain

---

## Abstract

Prostate cancer is reported to be the second most diagnosed cancer of men all over the world. In the last decades, new imaging techniques based on MRI have been developed improving the diagnosis task of radiologists. In practise, diagnosis can be affected by multiple factors reducing the chance to detect potential lesions. Computer-aided detection and computer-aided diagnosis have been designed to answer to these needs and provide help to radiologists in their daily duties. Research on computer-aided systems specifically focused for prostate cancer is a young technology and part of a dynamic research field for the last ten years. This survey aims to provide an overview of the researches carried out in this lapse of time and more precisely a comprehensive review of all the different stages composing the work-flow of a computer-aided system. We also provide a comparison between these studies and a discussion about the potential avenues for future research. In addition, we bring to the research community's knowledge the creation of a public online dataset aiming at providing solutions to the drawbacks identified in this survey.

**Keywords:** computer-aided detection, computer-aided diagnosis, prostate cancer, magnetic resonance imaging, magnetic resonance spectroscopy imaging, computer vision

---

## 1. Introduction

During the last century, physicists focused on constantly innovating in terms of imaging techniques assisting radiologists to overcome different tasks as cancer detection and diagnosis. However, human diagnosis still suffers from low repeatability, synonymous with erroneous detection or interpretations of abnormalities throughout clinical decisions ([61, 69]). These errors are driven by two majors causes ([61]). On the one hand, observer limitations (e.g., constrained human visual perception, fatigue or distraction) are the

---

\*Corresponding author.

Email addresses: guillaume.lemaitre@udg.edu (Guillaume Lemaître), marly@eia.udg.edu (Robert Martí), jordif@eia.udg.edu (Jordi Freixenet), pwalker@u-bourgogne.fr (Paul M. Walker), fabrice.meriaudeau@u-bourgogne.fr (Fabrice Meriaudeau)

principal human issues. On the other hand, the second reason is linked to the clinical cases themselves, for instance due to unbalanced data (number of healthy cases more abundant than malignant cases) or overlapping structures resulting from limitations of imaging techniques.

Computer vision has given rise to many promising solutions, but, instead of focusing on fully automatic computerized systems, researchers have aimed at providing computer image analysis techniques to aid radiologists in their clinical decisions ([61]). In fact, these investigations brought about both concepts of computer-aided detection (CADE) and computer-aided diagnosis (CADx) grouped under the acronym CAD. Since those first steps, evidence has shown that CAD systems enhance the diagnosis performance of radiologists. [28] reported a significant 4 % improvement in breast cancer detection, in accordance with later studies ([43]). Similar conclusions were drawn in the case of lung nodule detection ([100]), colon cancer ([151]) and prostate cancer (CaP) as well ([69]). [28] also hypothesized that CAD systems will be even more efficient assisting inexperienced radiologists than senior radiologists. That hypothesis was tested by [69] and was confirmed in case of CaP detection. In this particular study, inexperienced radiologists obtained equivalent performance to senior radiologists, both with the help of a CAD system whereas the accuracy of their diagnosis was significantly poorer without this assistance.

In contradiction with the aforementioned statement, CaP detection using CAD is a young technology due to the fact that magnetic resonance imaging (MRI) is the keystone medical imaging technique ([72]). Four distinct MRI modalities are employed in CAD for CaP and were mainly developed after the mid-1990s: (i) T<sub>2</sub> Weighted (T<sub>2</sub>-W) MRI ([77]), (ii) dynamic contrast-enhanced (DCE) MRI ([78]), (iii) magnetic resonance spectroscopy imaging (MRSI) ([93]) and (iv) diffusion weighted (DW) MRI ([170]). It can be noted that these techniques came into existence relatively recently mainly due to technological progress. In addition, the increase of magnetic field strength and the development of endorectal coil, both improved image spatial resolution ([184]) needed to perform more accurate diagnosis. It is for this matter that development of CAD for CaP is still lagging behind the other fields stated above.

The first study using MRI as inputs of a CAD system was published eleven years ago by [29]. Despite this, no less than fifty studies have been reviewed for this survey since that seminal work. To the best of our knowledge, there is no review in the literature regarding the advancement of CAD systems devoted specifically to CaP detection and diagnosis. Thus, our aim with this survey is threefold: (i) provide an overview of developed CAD systems for CaP detection and diagnosis based on MRI modalities (ii) assess the different work and (iii) point out avenues for future work.

We also would like to emphasize the fact that this study will review all the details of the computer vision aspects of the different studies. Thus, this survey is more intended for a medical imaging audience rather than a purely experimented clinical audience.

As discussed further in Sect. 2.2.3, we identified and characterized a common framework regarding the CAD systems. Stages involved in CAD work-flow can be categorized into three distinctive processes: (i)

image regularization, (ii) CADe, (iii) CADx (see Fig. 1). Image regularisation focuses on formatting the data while CADe and CADx allow to detect possible lesions and distinguish malignant from non-malignant tumours, respectively.

This paper is organized as follows: Sect. 2 deals with general information about human prostate and background about CaP. Methods regarding CaP screening and imaging techniques used are also presented as well as an introduction to the CAD framework. Sections 3 - 4 review techniques used in different steps involved in a CAD work-flow which will be our main contribution. Image regularization framework including pre-processing (Sect. 3.1), segmentation (Sect. 3.2) and registration (Sect. 3.3) will be covered as well as CADe and CADx strategies (Sect. 4) identified. Results and discussion are reported in Sect. 5 followed by a concluding section. Deriving from this discussion, we made available to the research community a public online dataset aiming at overcoming some drawbacks risen during the discussion.

## 2. Background

This section provides an overview of CaP as well as its detection and diagnosis. Subsequently a discussion of the current screening strategy for CaP and its drawbacks is presented. MRI plays an important role in improving the current strategy and a more detailed description of MRI modalities is given. Furthermore, a discussion regarding the aim of CAD systems will be given.

### 2.1. Prostate carcinoma

CaP has been reported on a worldwide scale to be the second most frequently diagnosed cancer of men accounting for 13.6% ([50]). Statistically, in 2008, the number of new diagnosed cases was estimated to be 899,000 with no less than 258,100 deaths ([50]). In United States, aside from skin cancer, CaP was declared to be the most commonly diagnosed cancer among men, implying that approximately one in six men will be diagnosed with CaP during their lifetime and one in thirty-six will die from this disease causing CaP to be the second most common cause of cancer death among men ([176], [6]).

Despite active research to determine the causes of prostate cancer, a fuzzy list of risk factors has been established ([5]). The etiology was linked to the following factors ([5]): (i) family history ([62, 180]), (ii) genetic factors ([1, 9, 53]), (iii) race-ethnicity ([62, 75]), (iv) diet ([4, 62, 116]), (v) obesity ([62, 164]). This list of risk factors alone cannot be used to diagnose CaP and in this way, screening enables early detection and treatment.

CaP growth is characterized by two main types of evolution ([181]): slow and fast. The slow-growing tumours, accounting for up to 85 % of all CaPs ([114]), progress slowly and usually stay confined to the prostate gland. For such cases, treatment can be substituted with active surveillance. In contrast, the second variant of CaPs develops rapidly and metastasises from prostate gland to other organs, primarily the

bones ([142]). Bone metastases, being an incurable disease, significantly affect the morbidity and mortality rate ([219]). Hence, the results of the surveillance have to be trustworthy in order to distinguish aggressive from slow-growing CaP.

CaP is more likely to develop in specific regions of the prostate. In that respect, around 70-80 % of CaPs originate in peripheral zone (PZ) whereas 10-20 % in transitional zone (TZ) ([26, 124, 179]). Only about 5 % of CaPs occur in central zone (CZ) ([35, 124]). However, those cancers appear to be more aggressive and more likely to invade other organs due to their location ([35]).

## *2.2. CaP screening and imaging techniques*

### *2.2.1. Current CaP screening*

Current CaP screening consists of three different stages. First, prostate-specific antigen (PSA) control is performed to distinguish between low and high risk CaP. Then, for confirmation, samples are taken during prostate biopsy and finally analysed to evaluate the prognosis and the stage of CaP. In this section, we present a detailed description of the current screening as well as its drawbacks.

Since its introduction in mid-1980s, PSA is widely used for CaP screening ([49]). A higher-than-normal level of PSA can indicate an abnormality of the prostate either as a benign prostatic hyperplasia (BPH) or a cancer ([74]). However, other factors can lead to an increased PSA level such as prostate infections, irritations, a recent ejaculation or a recent rectal examination ([147]).

A transrectal ultrasound (TRUS) biopsy is carried out for cases which are considered as pathological. At least six different samples are taken randomly from the right and left parts of three three different zones: apex, median and base. These samples are further evaluated using the Gleason grading system ([64]). Also, it should be noted that biopsy is an invasive procedure which can result in serious infection or urine retention ([34, 70]).

Although PSA screening has been shown to improve early detection of CaP ([34]), its lack of reliability motivates further investigations using MRI. Two reliable studies, carried out in the United States ([10]) and in Europe ([79, 173]), have attempted to assess the impact of early detection of CaP, with diverging outcomes ([34, 73]). The study carried out in Europe<sup>1</sup> concluded that PSA screening reduces CaP-related mortality by 21-44% ([79, 173]), while the American<sup>2</sup> trial found no such effect ([10]). However, both studies agree that PSA screening suffers from low specificity, with an estimated rate of 36 % ([172]). Both studies also agree that over-treatment is an issue: decision making regarding treatment is further complicated by difficulties in evaluating the aggressiveness and progression of CaP ([45]).

---

<sup>1</sup>The European Randomized Study of Screening for Prostate Cancer (ERSPC) started in the 1990s in order to evaluate the effect of PSA screening on mortality rate.

<sup>2</sup>The Prostate Lung Colorectal and Ovarian (PLCO) cancer screening trial is carried out in the United States and intends to ascertain the effects of screening on mortality rate.

Hence, new screening methods should be developed with improved specificity of detection as well as more accurate risk assessment (aggressiveness and progression). Current research is focused on identifying new biological markers to replace PSA-based screening ([21, 23, 132]). Until such research comes to fruition, these needs can be met through active-surveillance strategy using multi-parametric MRI techniques ([74, 131]). An MRI-CAD system, which is an area of active research and forms the focus of this paper, can be incorporated into this screening strategy allowing a more systematic and rigorous follow-up.

Another weakness of the current screening strategy lies in the fact that TRUS biopsy does not provide trustworthy results. Due to its “blind” nature imposed by the a random sampling strategy, there is a chance of missing aggressive tumours or detecting microfocal “cancers”, which influences the aggressiveness-assessment procedure ([136]). As a consequence, over-diagnosis is estimated at up to 30 % ([67]), while missing clinically significant CaP is estimated at up to 35 % ([185]). In an effort to solve both issues, alternative biopsy approaches have been explored. MRI/ultrasound (US)-guided biopsy has been shown to outperform standard TRUS biopsy ([44]). There, multimodal MRI images are fused with US images in order to improve localization and aggressiveness assessment to carry out biopsies. Human interaction plays a major role in biopsy sampling which can lead to low repeatability; by reducing potential human errors at this stage, the CAD framework can be used to improve repeatability of examination.

CaP detection and diagnosis benefit from the use of CAD and MRI techniques. In the following sections, these techniques will be presented in addition to an overview of CAD for CaP.

### 2.2.2. MRI imaging techniques

MRI provides promising imaging techniques to overcome the previous mentioned drawbacks. Unlike TRUS biopsy, MRI examination is a non-invasive protocol and has been shown to be the most accurate and harmless technique currently available ([199]). In this section, we review different MRI modalities developed for CaP detection and diagnosis. Features used by the radiologist in their daily diagnosis task will receive particular attention together with their drawbacks. Moreover, these features commonly form the basis for developing analytic tools and automatic algorithms. However, we refer the reader to Sect. 4.2 for more details on automatic feature detection methods since they are part and parcel of the CAD framework. Table 2.2.2 provides an overview of the following discussion.

- **$T_2$ -W MRI:**  $T_2$ -W MRI was the first MRI-modality used to perform CaP diagnosis using MRI ([77]). Nowadays, radiologists make use of it for CaP detection, localization and staging purposes. This imaging technique is well suited to render zonal anatomy of the prostate ([15]).

PZ and CG tissues are well perceptible in these images. The former is characterized by an intermediate/high-SI while the latter is depicted by a low-SI ([76]). An example of a healthy prostate is shown in Fig. 2(a).

In PZ, round or ill-defined low-SI masses are synonymous with CaPs ([77]) as shown in Fig. 2(b). Detecting CaP in CG is more challenging. In fact both normal CG tissue and malignant tissue, have a

Table 1: Overview of the features associated with each MRI modality used for medical diagnosis by radiologists. Acronyms: prostate cancer (CaP) - signal intensity (SI) - Gleason score (GS).

Modality	Significant features	CaP	Healthy tissue	GS correlation
T <sub>2</sub> -W MRI	SI	low-SI	intermediate to high-SI	+
T <sub>2</sub> map	SI	low-SI	intermediate to high-SI	+
DCE MRI	Semi-quantitative features:			
	– wash-in	faster	slower	0
	– wash-out	faster	slower	0
	– integral under the curve	higher	lower	0
	– maximum signal intensity	higher	lower	0
	– time-to-peak enhancement	faster	slower	0
	Quantitative features (Tofts' parameters):			
	– $k_{ep}$	higher	lower	0
	– $K^{trans}$	higher	lower	0
DW MRI	SI	higher-SI	lower-SI	+
ADC map	SI	low-SI	high-SI	+
MRSI	Metabolites:			
	Citrate (2.64 ppm)	lower concentration	higher concentration	+
	Choline (3.21 ppm)	higher concentration	lower concentration	0
	Spermine (3.11 ppm)	lower concentration	higher concentration	+

Notes:

+ = significantly correlated.

0 = no correlation.

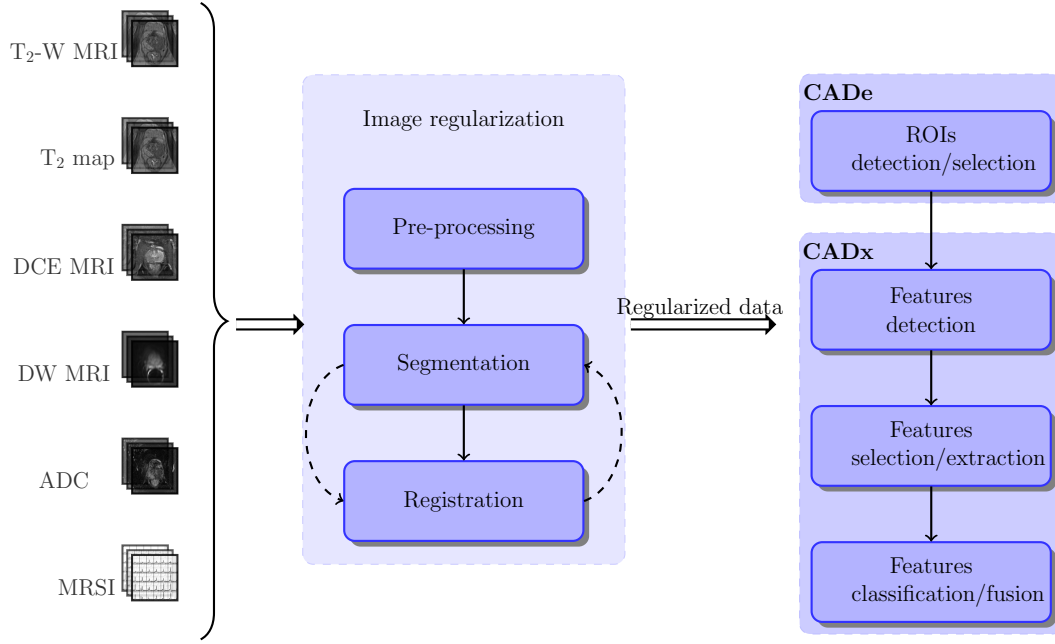
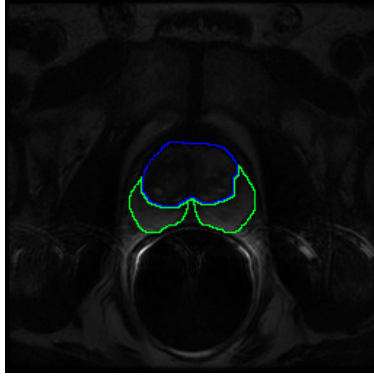
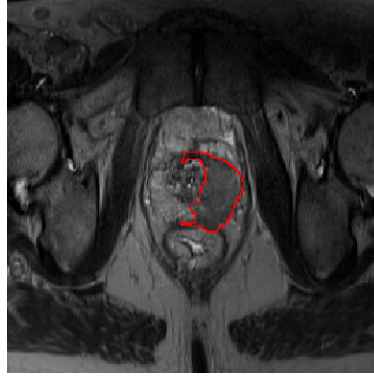


Figure 1: Common CAD framework based on MRI images used to detect CaP.



(a) T<sub>2</sub>-W-MRI slice of an healthy prostate acquire with a 1.5 Tesla MRI. The blue contour represents the CG while the PZ corresponds to the green contour.



(b) T<sub>2</sub>-W-MRI slice of a prostate with a CaP highlighted in the PZ using a 3.0 Tesla MRI scanner.



(c) T<sub>2</sub>-W-MRI slice of a prostate with a CaP highlighted in the CG using a 3.0 Tesla MRI scanner.

Figure 2: Rendering of T<sub>2</sub>-W-MRI prostate image with both 1.5 and 3.0 Tesla MRI scanner.

low-SI in  $T_2$ -W MRI reinforcing difficulties to distinguish between them. However, CaPs in CG appear often as homogeneous mass possessing ill-defined edges with lenticular or “water-drop” shapes ([3, 15]) as depicted in Fig. 2(c).

CaP aggressiveness was shown to be inversely correlated with SI. Indeed, CaPs assessed with a GS of 4-5 implied lower SI than the one with a GS of 2-3 ([217]).

In spite of the availability of these useful and encouraging features, the  $T_2$ -W modality lacks reliability ([74, 89]). Sensitivity is affected by the difficulties in detecting cancers in CG ([89]) while specificity rate is highly affected by outliers ([15]). In fact, various conditions emulate patterns of CaP such as BPH, post-biopsy haemorrhage, atrophy, scars and post-treatment ([15, 40, 76, 160, 170]). These issues can be partly addressed using more innovative and advanced modalities such as later presented.

- **$T_2$  Map:** As previously mentioned,  $T_2$ -W MRI modality shows low sensitivity due to various effects ([72]). However,  $T_2$  values alone have been shown to be more discriminative ([111]) and highly correlated with citrate concentration, a biological marker in CaP ([103, 104]).

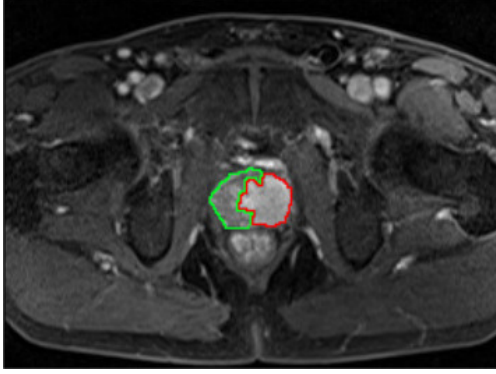
The Fast Spin-Echo (FSE) sequence has been shown to be particularly well suited in order to build a  $T_2$  map and obtain accurate  $T_2$  values ([102]).

Similar to  $T_2$ -W MRI,  $T_2$  values associated with CaP are significantly lower than those of healthy tissues ([60, 103]).

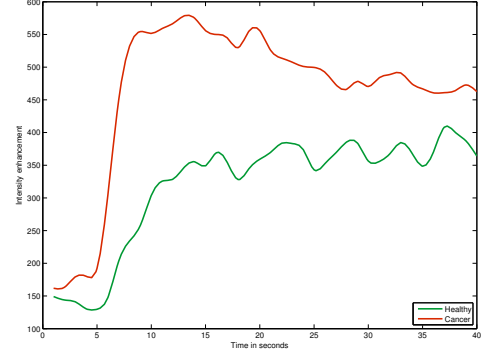
- **DCE MRI:** DCE MRI is an imaging technique which exploits the vascularity characteristic of tissues. Contrast media, usually gadolinium-based, is injected intravenously into the patient. The media extravasates from vessels to the extravascular-extracellular space (EES) and is then released back into the vasculature before being eliminated by the kidneys ([66]). Furthermore, the diffusion speed of the contrast agent may vary due to several parameters: (i) the permeability of the micro-vessels, (ii) their surface area and (iii) the blood flow ([145]).

DCE MRI is based on an acquisition of a set of  $T_1$  Weighted ( $T_1$ -W) MRI images over time. the Gadolinium-based contrast agent shortens  $T_1$  relaxation time enhancing contrast in  $T_1$ -W MRI images. The aim is to post-analyse the pharmacokinetic behaviour of the contrast media concentration in prostate tissues ([203]). The image analysis is carried out in two dimensions: (i) in the spatial domain on a pixel-by-pixel basis and (ii) in the time domain corresponding to the consecutive images acquired with the MRI. Thus, for each spatial location, a signal linked to contrast media concentration is measured as shown in Fig. 3 ([194]). CaPs are characterized by a signal having an earlier and faster enhancement as well as an earlier wash-out (cf., the rate of the contrast agent flowing out of the tissue) (see Fig. 3(b)) ([203]). Three different approaches exist to analyse these signals with the aim of tagging them as corresponding to either normal or malignant tissues. Qualitative analysis is based on assessment of the signal shape ([74]).





(a) T<sub>1</sub>-W-MRI image where the cancer is delimited by the red contour. The green area was still not invaded by the CaP



(b) Enhancement curve computed during the DCE-MRI analysis. The red curve is typical from CaP cancer while the green curve is characteristic of healthy tissue.

Figure 3: Illustration of typical enhancement signal observed in DCE-MRI analysis collected with a 3.0 Tesla MRI scanner.

Quantitative approaches consist of inferring pharmacokinetic parameter values ([194]). Those parameters are part of mathematical-pharmacokinetic models which are directly based on physiological exchanges between vessels and EES. The last family of methods mix both approaches and are grouped together under the heading of semi-quantitative methods. They rely on shape characterization using mathematical modelling to extract a set of parameters. These parameters will be discussed in a later section (see Fig. 11) ([74, 203]). It was shown that semi-quantitative and quantitative methods improve localization of CaP when compared with qualitative methods ([165]). Section 4.2.2 provides a full description of quantitative and semi-quantitative approaches.

DCE MRI combined with T<sub>2</sub>-W MRI has shown to enhance sensitivity compared to T<sub>2</sub>-W MRI alone ([83, 88, 171, 220]). Despite this fact, DCE MRI possesses some drawbacks. Due to its “dynamic” nature, patient motions during the image acquisition may lead to spatial misregistration of the image set ([203]). Furthermore, it has been suggested that malignant tumours are difficult to distinguish from prostatitis located in PZ and BPH located in CG ([74, 203]) as these two pairs of tissues tend to have similar appearances. Later studies have shown that CaPs in CG do not always manifest in homogeneous fashion. Indeed, tumours in this zone can present both hypo-vascularization and hyper-vascularization which illustrates the challenge of CaP detection in CG ([135]).

- **DW MRI:** As previously mentioned in the introduction, DW MRI is the most recent MRI imaging technique aiming at CaP detection and diagnosis ([170]). This modality exploits the variations in the motion of water molecules in different tissues ([92, 96]).

From the nuclear magnetic resonance (NMR) principle side, DW MRI sequence produces contrasted

images due to variation of water molecules motion. The method is based on the fact that the signal in DW MRI images is inversely correlated to the degree of random motion of water molecules ([81]). A higher degree of random motion results in a more significant signal loss whereas a lower degree of random motion is synonymous with lower signal loss ([81]). Under these conditions, the MRI signal is measured as:

$$M_{x,y}(t, b) = M_{x,y}(0) \exp\left(-\frac{t}{T_2}\right) S_{\text{ADC}}(b) , \quad (1)$$

$$S_{\text{ADC}}(b) = \exp(-b \times \text{ADC}) , \quad (2)$$

where  $S_{\text{ADC}}$  refers to signal drop due to diffusion effect, ADC is the apparent diffusion coefficient and  $b$  is the attenuation coefficient depending only on gradient pulses parameters: (i) gradient intensity and (ii) gradient duration ([97]).

By using this formulation, image acquisition with a parameter  $b = 0 \text{ s.mm}^{-2}$  corresponds to a  $T_2$ -W MRI acquisition. Then, increasing the attenuation coefficient  $b$  (cf., increase gradient intensity and duration) enhances the contrast in DW MRI images.

To summarize, in DW MRI images, CaPs are characterized by high-SI compared to normal tissues in PZ and CG as shown in Fig. 4(a) ([15]). However, some tissues in CG can look similar to CaP with higher SI ([15]).

Diagnosis using DW MRI combined with  $T_2$ -W MRI has shown a significant improvement compared with  $T_2$ -W MRI alone and provides highly contrasted images ([33, 146, 175]). As drawbacks, this modality suffers from poor spatial resolution and low specificity due to false positive detection ([33]).

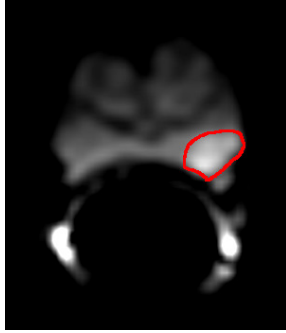
With a view to eliminate these drawbacks, radiologists are extracting quantitative maps from DW MRI. This imaging technique is presented next.

- **ADC Map:** The NMR signal measured for DW MRI images is not only affected by diffusion as shown in Eq. (1). However, the signal drop (Eq. (2)) is formulated such that the only variable is the acquisition parameter  $b$  ([97]). The ADC is considered as a “pure” diffusion coefficient and can be extracted to build a quantitative map.

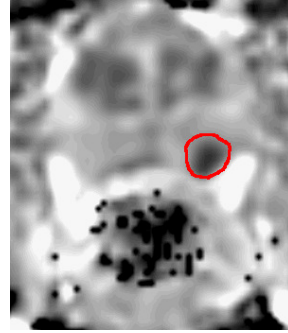
From Eq. 1, it is clear that performing multiple acquisitions only varying  $b$  will not have any effect on the term  $M_{x,y}(0) \exp\left(-\frac{t}{T_2}\right)$ . Thus, Eq. 1 can be rewritten as:

$$S(b) = S_0 \exp(-b \times \text{ADC}) . \quad (3)$$

To compute the ADC map, a minimum of two acquisitions are necessary: (i) for  $b_0 = 0 \text{ s.mm}^{-2}$  where the measured signal is equal to  $S_0$ , and (ii)  $b_1 > 0 \text{ s.mm}^{-2}$  (typically  $1000 \text{ s.mm}^{-2}$ ). Then, the ADC



(a) DW-MRI image. The cancer corresponds to the high SI region highlighted in red.



(b) ADC map computer. The cancer corresponds to the low SI region highlighted in red.

Figure 4: Illustration of of DW-MRI and ADC map. The signal intensity corresponding to cancer are inversely correlated on these two types of imaging techniques.

map can be computed as:

$$\text{ADC} = -\frac{\ln\left(\frac{S(b_1)}{S_0}\right)}{b_1}. \quad (4)$$

More accurate computation of the ADC map can be obtained by performing several acquisitions with different values for the parameter  $b$  and performing a semi-logarithmic linear fitting using the model presented in Eq. (3).

Regarding the appearance of the ADC maps, it was previously stated that by increasing the value of  $b$ , the signal of CaP tissue increases significantly. From Eq. (4), it can be shown that tissue appearance in the ADC map will be the inverse of DW MRI images. Then, CaP tissue is associated with low-SI whereas healthy tissue appears brighter as depicted in Fig. 4(b) ([15]).

Similar to the gain achieved by DW MRI, diagnosis using ADC map combined with T<sub>2</sub>-W MRI significantly outperforms T<sub>2</sub>-W MRI alone ([33, 47]). Moreover, it has been shown that ADC is correlated with GS ([68, 82, 150]).

However, some tissues of the CG zone mimic CaP with low-SI ([89]) and image distortion can arise due to haemorrhage ([33]). It has also been noted that a high variability of the ADC occurs between different patients making it difficult to define a static threshold to distinguish CaP from non-malignant tumours ([33]).

- **MRSI:** CaP induces metabolic changes in the prostate compared with healthy tissue. Thus, CaP detection can be carried out by tracking changes of metabolite concentration in prostate tissue. MRSI is an

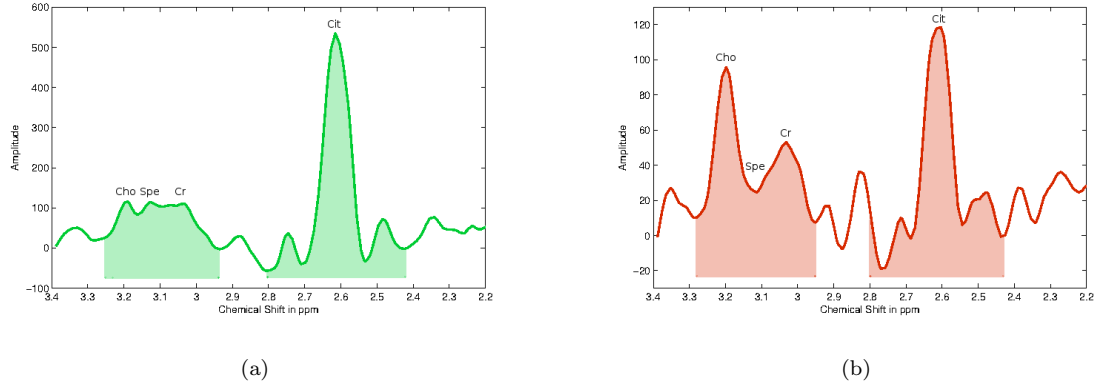


Figure 5: Illustration of an MRSI spectrum both healthy (Fig. 5(a)) and cancerous (Fig. 5(b)) voxel with a 3.0 Tesla MRI. The highlighted areas corresponds to the related concentration of the metabolites which is computed by integrating the area under each peak. Acronyms: Choline (Cho), Spermine (Spe), Creatine (Cr) and Citrate (Cit).

NMR-based technique which generates spectra of relative metabolite concentration in a region of interest (ROI).

In order to track changes of metabolite concentration, it is important to know which metabolites are associated with CaP. To address this question, clinical studies identified three biological markers: (i) citrate, (ii) choline and (iii) polyamines composed mainly of spermine, and in less abundance of spermidine and putrescine ([14, 39, 63]).

An increased concentration of choline associated with a decreased concentration of citrate and spermine are related to the presence of CaP ([14, 39, 63, 65]).

To determine the concentration of these biological markers, one has to focus on the MRSI modality. In each spectrum acquired, each peak is associated with a particular metabolite and the area under each peak corresponds to the relative concentration of this metabolite (see Fig. 5) ([147]).

Hence, frequencies of interest in regard to CaP detection and diagnosis should correspond to the earlier mentioned metabolites. Choline and spermine are represented by a single peak at respectively 3.21 ppm and 3.11 ppm ([202]). Due to the coupling effect, citrate is represented by three or four peaks depending on the magnetic field strength. Citrate ranges from 2.47 ppm to 2.81 ppm with a central frequency at 2.64 ppm ([202]). Then, relative concentrations of these metabolites are obtained by computing the area under the curve of the spectrum between the lower and upper frequency limits of each peak (see Fig. 5). It can be noted that a creatine peak is located at 3.02 ppm and the three metabolite peaks tend to be merged together at clinical magnetic field strengths (see Fig. 5) ([65, 74]).

MRSI allows examination with high specificity and sensitivity compared to other MRI modalities ([33]). Furthermore, it has been shown that combining MRSI with MRI improves detection and diagnosis performance ([86, 169, 204]). Citrate and spermine concentrations are inversely correlated with the GS

allowing us to distinguish low from high grade CaPs ([63]). However, choline concentration does not provide the same properties ([63]).

Table 2: Overview of the different studies reviewed with their main characteristics. Acronyms: number (#) - image regularization (Img. Reg.).

Index	Study	# patients	MRI-modality				Strength of field		Studied zones		CAD stages		
			T <sub>2</sub> -W MRI	DCE MRI	DW MRI	MRSI	1.5 T	3.0 T	PZ	CG	Img. Reg.	CADe	CADx
[1]	[7]	25	✓	✓	✗	✗	✓	✗	✓	✗	✓!	✗	✓
[2]	[8]	25	✓	✓	✗	✗	✓	✗	✓	✗	✓!	✗	✓
[3]	[11]	53	✓	✗	✓	✗	✓	✗	✓	✓	✗	✗	✓
[4]	[13]	10	✓	✓	✓	✗	✓	✗	✓	✗	✗	✓	✓
[5]	[12]	21	✓	✓	✓	✗	✓	✗	✓	✗	✓!	✓	✓
[6]	[29]	15	✓	✗	✓	✗	✓	✗	✓	✗	✗	✗	✓
[7]	[59]	10	✓	✓	✓	✗	✓	✗	✓	✗	✓	✓	✓
[8]	[87]	24	✗	✗	✗	✓	✓	✗	✓	✓	✓!	✓	✓
[9]	[94]	25	✓	✓	✓	✗	✓	✗	✓	✗	✓!	✗	✓
[10]	[109]	188	✓	✓	✓	✗	✗	✓	✓	✗	✓!	✓	✓
[11]	[108]	288	✓	✓	✓	✗	✗	✓	✓	✓	✓!	✓	✓
[12]	[105]	347	✓	✓	✓	✗	✗	✓	✓	✓	✓!	✓	✓
[13]	[112]	11	✓	✓	✓	✗	✓	✗	✓	✗	✓!	✓	✓
[14]	[110]	54	✓	✓	✓	✗	✗	✓	✓	✓	✓!	✗	✓
[15]	[113]	27	✓	✗	✗	✗	✓	✗	✓	✗	✓!	✓	✓
[16]	[115]	55	✓	✗	✗	✗	✓	✗	✓	✗	✓!	✗	✓
[17]	[122]	18	✗	✗	✗	✓	✗	✓	✓	✓	✗	✓	✓
[18]	[123]	10	✗	✓	✗	✗	✓	✗	✓	✗	✓!	✓	✓
[19]	[134]	23	✓	✓	✓	✗	✓	✗	✓	✗	✓!	✗	✓
[20]	[133]	30	✓	✓	✓	✗	✓	✗	✓	✗	✓!	✗	✓
[21]	[143]	20	✓	✓	✓	✗	✓	✗	✓	✗	✓!	✓	✓
[22]	[144]	20	✓	✓	✓	✗	✓	✗	✓	✗	✓!	✓	✓
[23]	[148]	22	✗	✗	✗	✓	✗	✓	✓	✓	✓!	✓	✓
[24]	[150]	48	✓	✓	✓	✗	✗	✓	✓	✓	✗	✗	✓
[25]	[158]	100	✗	✓	✗	✗	✓	✗	✓	✓	✗	✗	✓
[26]	[183]	42	✗	✓	✗	✗	✗	✓	✓	✓	✗	✓	✓
[27]	[189]	14	✗	✗	✗	✓	✓	✗	✓	✓	✓!	✓	✓
[28]	[190]	18	✗	✗	✗	✓	✓	✗	✓	✓	✓!	✓	✓
[29]	[191]	18	✗	✗	✗	✓	✓	✗	✓	✓	✓!	✓	✓
[30]	[192]	15	✓	✗	✗	✓	✓	✗	✓	✓	✓!	✓	✓
[31]	[188]	19	✓	✗	✗	✓	✓	✗	✓	✓	✓!	✓	✓
[32]	[193]	36	✓	✗	✗	✓	✓	✗	✓	✓	✗	✓	✓
[33]	[187]	29	✓	✗	✗	✓	✓	✗	✓	✓	✓!	✓	✓
[34]	[209]	16	✓	✗	✗	✓	✓	✗	✓	✓	✗	✓	✓
[35]	[207]	6	✓	✓	✗	✗	✗	✓	✓	✓	✓!	✓	✓
[36]	[208]	6	✓	✓	✗	✗	✗	✓	✓	✓	✓	✓	✓
[37]	[206]	12	✓	✓	✓	✗	✗	✓	✓	✓	✓!	✓	✓
[38]	[210]	22	✓	✗	✗	✗	✗	✓	✓	✓	✓!	✓	✓
[39]	[212]	29	✓	✓	✗	✗	✓	✗	✓	✗	✓!	✗	✓
[40]	[214]	29	✗	✓	✗	✗	✓	✗	✓	✗	✓!	✗	✓
[41]	[213]	29	✓	✓	✗	✗	✓	✗	✓	✗	✓!	✗	✓
[42]	[211]	NA	✓	✓	✓	✗	✗	✓	✓	✗	✓!	✓	✓

Notes:

✗: not used or not implemented.

✓!: partially implemented.

✓: used or implemented.

Unfortunately, MRSI also presents several drawbacks. First, MRSI acquisition is time consuming which prevents this modality from being used in daily clinical practise ([15]). In addition, MRSI suffers from low spatial resolution due to the fact that signal-to-noise (SNR) is linked to the voxel size. However, this issue is addressed by developing new scanners with higher magnetic field strengths such as 7.5 T ([63]). Finally, a high variability of the relative concentrations between patients has been observed ([33]). The same observation was made depending on the zones studied (cf., PZ, CG, base, mid-gland, apex) ([98, 216]). Due to this variability, it is difficult to use a fixed thresholds in order to differentiate CaP from healthy tissue.

### 2.2.3. Computer-aided systems for CaP: CAdE - CAdx

As previously mentioned in the introduction (see Sect. 1), CADs are developed to advise and backup radiologists in their tasks of CaP detection and diagnosis; CADs are not aimed to provide fully automatic decisions ([61]). CADs can be divided into two different sub-groups either as CAdE, with the purpose to highlight probable lesions in MRI images, or CAdx, which focuses on differentiating malignant from non-malignant tumours ([61]). Moreover, an intuitive approach, motivated by developing a framework combining detection-diagnosis, is to mix both CAdE and CAdx by using the output of the former mentioned as a input of the latter named. Although the outcomes of these two systems should differ, the framework of both CAD systems is similar. The CAD work-flow is presented in Fig. 1.

MRI modalities mentioned in Sect. 2.2.2 are used as inputs of CAD for CaP. The images acquired from the different modalities show a large variability between patients: the prostate organ can be located at different positions in images (e.g., patient motion, variation of acquisition plan), and the SI can be corrupted with noise or artefacts during the acquisition process (eg., magnetic field inhomogeneity, use of endorectal coil). To address these issues, the first stage of CAD is to pre-process multiparametric MRI images to reduce noise, remove artefacts and standardize the SI. As most of the later processes will be only focused on the prostate. It is necessary to segment the prostate in each MRI-modality to define it as a ROI. However, data may suffer from misalignment due to patient motion or different acquisition parameters. Therefore, a registration step is usually performed so that all the previously segmented MRI images will be in the same reference frame. Registration and segmentation steps can be swapped depending on the strategy chosen.

Some studies do not fully apply the methodology depicted in Fig. 1. Details about those can be found in Tab. 2. Some studies preferred to work directly with raw data in order to demonstrate the robustness of their approaches to noise or artefacts. In some cases, prostate segmentation is performed manually as well as registration. It is also sometimes assumed that no patient motions occur during the acquisition procedure, removing the need of registering the multiparametric MRI images.

Once the data are regularized, it becomes possible to extract features and classify these data to obtain either the location of possible lesions (CAdE) or/and the malignancy nature of these lesions (CAdx).

In a CADe framework, *possible lesions will be segmented automatically* and further used as inputs of a CADx. Nevertheless, this is not the only case that CADe frameworks encountered. Some works also used a fused CADe-CADx framework in which a voxel-based delineation approach is used, allowing to obtain the location of the malignant lesions as results. On the other hand, manual lesions segmentation are not considered to be part of a CADe.

CADx is composed of the processes allowing to *distinguish malignant from non-malignant tumours*. In the studies reviewed, CaP malignancy is defined using the grade of the GS determined after post-biopsy or prostatectomy. As presented in Fig. 1, CADx is usually composed of the three common steps used in classification framework: (i) features detection, (ii) features extraction/selection and (iii) features classification.

As pointed out in the introduction, performance of CaP detection and diagnosis are affected by observer interpretation and limitations ([61, 69]). CAD offers a possible solution in order to reduce this variability. As mentioned in the introduction, the effects of CAD on the observer performance has been studied ([69]), with results showing that CADs benefit to less-experienced radiologist to perform similarly as experienced radiologist in their tasks ([69]).

### 2.3. Literature classification

The CAD review is organized using the methodology presented in Fig. 1. Methods embedded in the image regularization framework are presented before to focus on the image classification framework, the later being divided into CADe and CADx. Table 2 summarizes the forty-one different CAD studies reviewed in this paper. The first set of information reported is linked to the data acquisition such as the number of patients included in the study, the modalities acquired as well as the strength of the field of the scanner used. Subsequently, information about the prostate zones considered in the CAD analysis (PZ or CG) are reported since that detecting CaP in the CG is a more challenging problem and has received particular attention only in recent publications.

## 3. Image regularization framework

This section provides a review of the methods used in CADs in order to regularize input images. We start with pre-processing methods presented in Sect. 3.1, focusing mainly on the reduction of noise level and artefacts as well as standardization of SI. Sections 3.2 and 3.3 will be dedicated to segmentation methods, so that later methods only operate on the segmented prostate, and registration to align segmented images from different MRI-modalities in the same reference frame.



Table 3: Overview of the pre-processing methods used in CAD systems.

Pre-processing operations	References
<i>MRI pre-processing:</i>	
Noise filtering:	
Median filtering	[22-23]
Wavelet-based filtering	[1-2,15]
Bias correction:	
Parametric methods	[16,36]
Non-parametric methods	[37]
Standardization:	
Statistical-based normalization:	[3-4,16,21-22,36,38]
Organ SI-based normalization	[19-20]
<i>MRSI pre-processing:</i>	
Phase correction	[23]
Water and lipid residuals filtering	[8]
Baseline correction	[23,32]
Frequency alignment	[32]
Normalization	[23]

### 3.1. Pre-processing

#### 3.1.1. MRI images pre-processing

Three different groups of pre-processing methods are commonly applied to images as initial stage in CAD.

- **Noise filtering:** The NMR signal measured and recorded in the k-space during an MRI acquisition is affected by noise. This noise obeys a complex Gaussian white noise mainly due to thermal noises in the patient area ([137]). Furthermore, MRI images visualized by radiologists are in fact the magnitude images resulting from the complex Fourier transform of the k-space data. The complex Fourier transform, being a linear and orthogonal transform, does not affect the Gaussian noise characteristics ([137]). However, the function involved in the magnitude computation is a non-linear transform (i.e., the square root of the sum of squares of real and the imaginary parts), implying that the noise distribution is no longer Gaussian; it indeed follows a Rician distribution making the denoising task harder. Briefly, a Rician distribution can be characterized as follows: in low-SI region (low SNR), it can be approximated with a Rayleigh distribution while in high-SI region (high SNR), it is similar to a Gaussian distribution ([121]). Reviews of all denoising methods can be found in the work of [24] and [130].

Median filtering is the simplest approach used to address the denoising issue in MRI images ([143, 144]). However, from a theoretical point of view, this simple filtering method is not well formalized to address the noise distribution in MRI images.

More complex approaches were proposed to overcome this problem. A common method used to denoise MRI images is based on wavelet-based filtering. Investigations focus on the strategies to perform the most adequate coefficient shrinkage method (e.g., using thresholding, singularity property or Bayesian framework) ([153]).

[7, 8] performed wavelet shrinkage to denoise magnitude MRI images (cf., T<sub>2</sub>-W-MRI and DCE-MRI) using thresholding techniques ([120]). However, since the wavelet transform is an orthogonal transform, the Rician distribution of the noise is preserved in the wavelet-domain. Hence, for low SNR, the wavelet and scaling coefficients still suffer from a bias due to this specific noise distribution ([137]).

[113] used the filtering technique proposed by [154] to denoise T<sub>2</sub>-W-MRI which was based on joint detection and estimation theory ([126]).

- **Bias correction:** Besides being corrupted by noise, MRI images are also affected by the inhomogeneity of the MRI field commonly referred to as bias field ([182]). This bias field results in a smooth variation of the SI through the image. When an endorectal coil is used, an artefact resulting of an hyper-intense signal can be observed around the coil on the images. As a consequence, the SI of identical tissues varies depending on their spatial location in the image making further processes such as segmentation or registration harder ([85, 215]). A review of bias correction methods can be found in [215].

The model of image formation is usually formalized such that:

$$s(\mathbf{x}) = o(\mathbf{x})b(\mathbf{x}) + \eta(\mathbf{x}) , \quad (5)$$

where  $s(\mathbf{x})$  is the corrupted SI at the pixel for the image coordinates  $\mathbf{x} = \{x, y\}$ ,  $o(\mathbf{x})$  is the “noise-free signal” ,  $b(\mathbf{x})$  is the bias field function and  $\eta(\mathbf{x})$  is an additive white Gaussian noise.

Hence, the task of bias correction involves estimating the bias function  $b(\mathbf{x})$  in order to infer the “signal-free bias”  $o(\mathbf{x})$ .

[208] performed bias correction on T<sub>2</sub>-W-MRI using a parametric Legendre polynomial model proposed by [182] and available in the Insight Segmentation and Registration Toolkit (ITK) library<sup>3</sup>.

[115] corrected the inhomogeneity in T<sub>2</sub>-W-MRI images by using the method proposed by [117]. In this method, the MRI images are corrected iteratively by successively detecting the image foreground via generalized scale ( $g$ -scale) and estimating a bias field function based on a second-order polynomial model.

#### – ***SI normalization/standardization:***

As discussed in the later section, segmentation or classification tasks are usually performed by first learning from a training set of patients. Hence, one can emphasize the desire to perform MRI examinations with a high repeatability or in other words, one would like to obtain similar MRI images (cf., similar SIs) for patients of the same group (cf., healthy patients *vs.* patients with CaP), for a similar sequence.

However, it is a known fact that variability between patients occurs during the MRI examinations even using the same scanner, protocol or sequence parameters ([138]). Hence, the aim of normalization or standardization of the MRI data is to remove the variability between patients and enforce the repeatability of the MRI examinations.

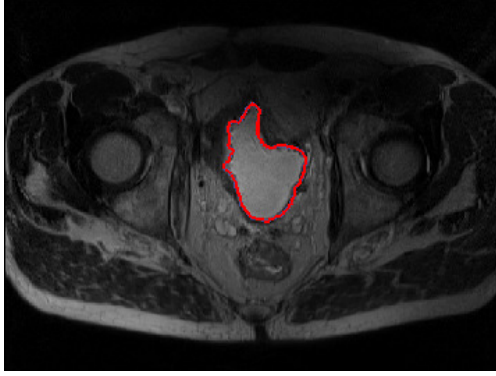
Approaches used to standardize MRI images can be either categorized as statistical-based standardization or organ SI-based standardization.

[12, 13] as well as [143, 144] standardized T<sub>2</sub>-W, DCE and DW MRI images by computing the *standard score* (also called *z-score*) of the pixels of the PZ. In a similar way, [110] normalized T<sub>2</sub>-W-MRI by making use of the median and interquartile range for all the pixels.

[115] scaled the SI of T<sub>2</sub>-W-MRI images using the method proposed by [139] based on probability density function (PDF) matching. This approach is based on the assumption that MRI images from the same sequence should share the same PDF appearance. Hence, one can approach this issue by transforming and matching the PDFs using some statistical landmarks such as median and different quantiles.

---

<sup>3</sup>The ITK library is available at: <http://www.itk.org/>



(a) Illustration and location of the bladder on a T<sub>2</sub>-W-MRI image acquired with a 3.0 Tesla MRI scanner



(b) Illustration and location of the femoral arteries on a T<sub>1</sub>-W-MRI image acquired with a 3.0 Tesla MRI scanner

Figure 6: Illustration of the two organs used by [133, 134] to normalize T<sub>2</sub>-W and T<sub>1</sub>-W MRI images.

[206, 208, 210] used a variant of this previous approach presented in the work of [118] aiming to standardize the T<sub>2</sub>-W-MRI images. Instead of computing the PDF of an entire image, a pre-segmentation of the foreground is carried out via  $g$ -scale.

The methods described above were statistical-based methods. However, the standardization problem can be tackled by normalizing the MRI images using the SI of some known organs present in these images. [133, 134] normalized T<sub>2</sub>-W-MRI images by dividing the original SI of the images by the mean SI of the bladder (see Fig. 6(a)). Likewise, [134] standardized the T<sub>1</sub>-W-MRI images using the arterial input function (AIF). They computed the AIF by taking the mean of the SI in the most enhanced part of the common femoral arteries (see Fig. 6(b)) as proposed by [218].

### 3.1.2. MRSI spectra

Presented in Sect. 2.2.2, MRSI is a modality related to a one dimensional signal. Hence, specific pre-processing steps for this type of signals have been applied instead of standard signal processing methods.

- **Phase correction:** MRSI data acquired suffer from zero-order and first-order phase misalignments as shown in Fig. 7 ([31, 141]).

[148] used a method proposed by [31] where the phase of MRSI signal is corrected based on entropy minimization in the frequency domain.

- **Water and lipid residuals filtering:** The water and lipid metabolites occur in much higher concentrations than the metabolites of interests (cf., choline, creatine and citrate) ([141, 222]). Fortunately, specific MRSI sequences were developed in order to suppress water and lipid metabolites using pre-saturation techniques ([222]). However, these techniques do not perfectly remove water and lipids peaks and some

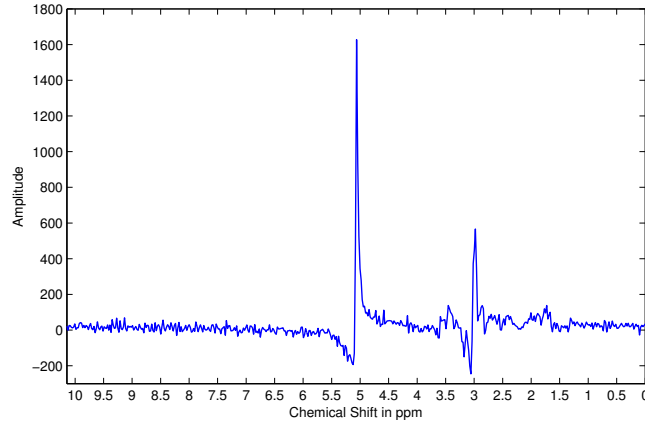


Figure 7: Illustration of frequency and phase misalignment in an MRSI spectra acquired with a 3.0 Tesla MRSI scanner. Focusing on the phase misalignment, note the distortion of the signal specially visible for the water (cf., around 5.1 ppm) and citrate (cf., around 3 ppm) peaks. Regarding the frequency misalignment, the water peak is known to be aligned at 4.65 ppm. However, it can be observed that this peak is occurring around 5.1 ppm.

residuals are still present in the MRSI spectra as shown in Fig. 8. Therefore, different post-processing methods have been proposed to enhance the quality of the MRSI spectra by removing these residuals.

[87] used the well known HSVD algorithm proposed by [152] which models the MRSI signal by a sum of exponentially damped sinusoids in the time domain.

- **Baseline correction:** Sometimes, the problem discussed in the above section regarding the lipid molecules is not addressed simultaneously with water residuals suppression. Lipids and macromolecules are known to affect the baseline of the MRSI spectra. They could cause errors during further fitting processes aiming to quantify the metabolites, especially regarding the citrate metabolite.

[148] made the comparison of two different methods to detect the baseline and correct the MRSI spectra which are based on the work of [101] and [46]. [101] addressed the problem of baseline detection in the frequency domain by iteratively fitting a polynomial of low degree.

[148] modified this algorithm by convolving a Gaussian kernel to smooth the MRSI signal instead of fitting a polynomial function.

Unlike [101], [46] proposed to correct the baseline in the time domain by multiplying the MRSI signal by a decreasing exponential function.

However, [148] concluded that the method proposed by [101] outperformed the one of [46]. In the contemporary work of [193], the authors detected the baseline using a local non-linear fitting method avoiding regions with significant peaks which were detected using an experimentally parametrised signal-to-noise ratio (i.e. a value larger than 5 dB).

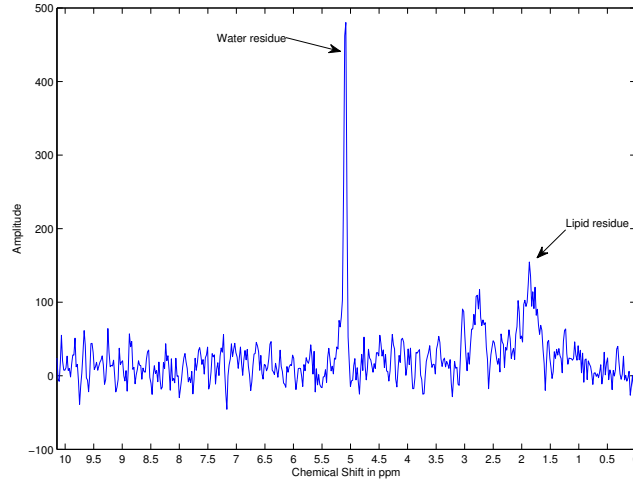


Figure 8: Illustration of the residues of water and fat even after their suppression during the acquisition protocol. The acquisition was carried out with a 3.0 Tesla MRI.

- **Frequency alignment:** Due to variations of the experimental conditions, a frequency shift can be observed in the MRSI spectra as shown in Fig. 7 ([31, 141]).

[193] corrected the frequency shift by first detecting known metabolite peaks such as choline, creatine and citrate. The frequency shift is corrected by minimizing the frequency error between the experimental and theoretical values of each of these peaks.

- **Normalization:** Due to variations of the experimental conditions, the MRSI signal may also vary between patients.

[148] as [46] compared two methods to normalize the MRSI signal. In each method, the original MRSI spectra is divided by a normalization factor, similar to the intensity normalization described earlier.

The first approach to obtain the normalization factor is based on an estimation of the water concentration. It is required to have an additional MRSI sequence where the water metabolites are unsuppressed. Using this sequence, an estimation of the water concentration can be performed using the previously reported HSVD algorithm. The second approach to normalization is based on using the  $L_2$  norm of the MRSI spectra  $\|s(\xi)\|_2$ . It should be noted that both [148] and [46] concluded that the  $L_2$  normalization was more efficient in their framework.

### 3.2. Segmentation

The segmentation task consists of delineating the prostate boundaries in the MRI. This procedure is of particular importance for focusing the posterior processing on the organ of interest ([58]). In this section, only the segmentation methods used in CAD systems are presented and summarized in Tab. 4. An exhaustive

Table 4: Overview of the segmentation methods used in CAD systems.

Segmentation methods	References
<i>MRI-based segmentation:</i>	
Manual segmentation	[4-5,17,19-22,25,39-41]
Region-based segmentation	[11-12]
Model-based segmentation	[10,35-37,42]
<i>MRSI-based segmentation:</i>	
Clustering	[29]

review of prostate segmentation methods in MRI can be found in [58] as well as prostate modelling in [32].

### 3.2.1. MRI-based segmentation

- **Manual segmentation:** To highlight the importance of prostate segmentation task in CAD systems, it is interesting to note the large number of studies which segment manually the prostate organs ([12, 13, 122, 133, 134, 143, 144, 158, 212, 214]). In all the cases, the boundaries of the prostate gland are defined in order to limit the further processing to only this area. This approach ensures the right delineation of the organ nevertheless this procedure is highly time consuming and should be performed by a radiologist.
- **Atlas-based segmentation:** [108] used a multi-atlas-based segmentation ([91]) using multi-modal images (e.g., T<sub>2</sub>-W-MRI and ADC map) to segment the prostate with an additional pattern recognition method to differentiate CG and PZ as proposed in [106]. This method consists of three different steps: (i) the registration between each atlas and the multi-modal images, (ii) the atlas selection and finally (iii) the classification of the prostate segmented voxels in either CG or PZ.

[105] used an almost identical algorithm proposed in PROMISE12 challenge ([107]). Their segmentation method is also based on multi-atlas multi-modal images. However, SIMPLE method ([95]) is used to combine labels after the registration of the different atlas to obtain the final segmentation.

- **Model-based segmentation:** [207, 208] used the multi-attribute non-initializing texture reconstruction based active shape model (MANTRA) method as proposed by [196]. MANTRA is closely related to the active shape model (ASM) from [38]. This algorithm consists of two stages: (i) a training stage where a shape and appearance model is generated and (ii) the actual segmentation performed based on the learned model.

[109] and [211] used an approach proposed by [80] in which the bladder, prostate and rectum are segmented. The segmentation task is performed as an optimization problem taking into account three parameters into account linked to organs such as: (i) the shape, (ii) the location and (iii) the respective

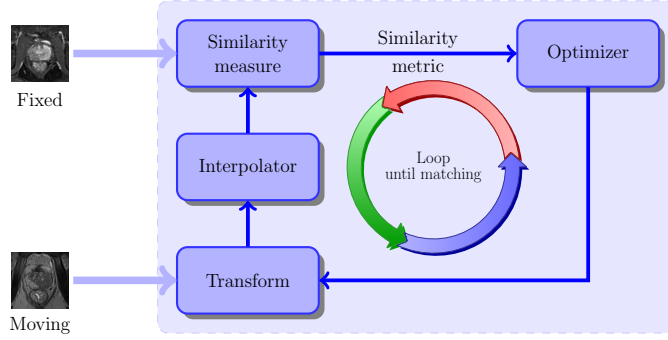


Figure 9: Typical framework involved to solve the registration problem.

angles between them. Furthermore, [109] used only ADC map to encode the appearance whereas [211] used both ADC and  $T_2$  maps.

### 3.2.2. MRSI-based segmentation

[191] localized the voxels corresponding to the prostate organ using a hierarchical spectral clustering. First, each MRSI spectrum is projected into a lower dimension space using graph embedding ([174]).

### 3.3. Registration

Table 5: Classification of the different registration methods used in the CAD systems reviewed. Acronyms: gradient descent (GD), Nelder-Mead (NM).

Study index	Modality registered	Type	Geometric model		Similarity measure			Optimizer	
			Affine	Elastic	MSE	MI	CMI	GD	L-BFGS-B
[1-2]	$T_2$ -W - DCE	2D	✓	—	✓	—	—	—	—
[7]	$T_2$ -W - DW	2D	✓	✓	—	—	—	—	—
[7]	$T_2$ -W - DCE	2D	✓	✓	—	✓	—	✓	—
[35-36]	$T_2$ -W - DCE	2D	✓	—	—	✓	—	—	—
[37]	$T_2$ -W - DCE - DW	3D	✓	—	—	—	✓	✓	—
[39]	$T_2$ -W - DCE	3D	✓	—	—	✓	—	—	—
[41]	$T_2$ -W - DCE	3D	✓	✓	—	✓	—	—	✓

Notes:

—: not used or not mentioned.

✓: used or implemented.

The role of image registration is vital in CAD systems using multi-parametric MRI images. As it will be discussed in Sect. 4, for the sake of an optimal classification, the features detected in each modality



will be grouped depending of their spatial locations. Hence, one has to ensure the perfect alignment of the multi-modal MRI images ahead of performing any classification scheme.

Image registration is the procedure consisting of aligning an unregistered image (also called moving image) into a template image (also called fixed image) via a geometric transformation. This problem is usually addressed as presented in Fig. 9. An iterative procedure takes place to infer the geometric transformation (parametric or non-parametric) via an optimizer, which maximizes the similarity between the two images.

From Sect. 3.3.1 to 3.3.4, we individually review the different components of a typical registration framework (Fig 9). Section 3.3.5 will summarize the combinations of these components especially for the frameworks used in CAD systems. Exhaustive reviews covering all registration methods in computer science and medical fields can be found in [119] and [223], respectively.

### 3.3.1. Geometric transformation models

As previously mentioned, the registration problem is to align two images or volumes by finding the geometric transformation. Regarding the transformation, from all CAD systems reviewed, only parametric methods have been implemented.

Two different groups of parametric transformation models have been used, each of them are characterized by the degree of freedom that they offer.

Affine transformations provide four degrees of freedom managing rotations and translation as with the rigid transformations but also shearing and scaling. Hence, for a 2D space where  $\mathbf{x} = (x, y) \in \mathbb{R}^2$ , an affine transformation  $\mathcal{T}_A$  is formalized as:

$$\begin{aligned} \mathcal{T}_A(\mathbf{x}) &= \begin{bmatrix} A & \mathbf{t} \\ \mathbf{0}^T & 1 \end{bmatrix} \mathbf{x} , \\ &= \begin{bmatrix} a_{11} & a_{12} & t_x \\ a_{21} & a_{22} & t_y \\ 0 & 0 & 1 \end{bmatrix} \begin{bmatrix} x \\ y \\ 1 \end{bmatrix} , \end{aligned} \tag{6}$$

Hence the four parameters  $\{a_{11}, a_{12}, a_{21}, a_{22}\}$  of the affine matrix and  $\{t_x, t_y\}$  of the translation encode an affine transformation.

In the case of 3D registration using image volumes, an additional component  $z$  has to be taken into account such that  $\mathbf{x} = (x, y, z)$ . Thus the geometric transformation  $\mathcal{T}_A(\cdot)$  is of size  $4 \times 4$  with nine parameters involved.

The other group of transformations is known as elastic transformations and offer the advantage to handle local distortions. In the reviewed CAD systems, the radial basis functions are used to formalize the local distortions such as:

$$\mathcal{T}_E(\mathbf{x}) = \frac{a_{11}x - a_{12}y + t_x + \sum_i c_i g(\|\mathbf{x} - p_i\|)}{a_{21}x + a_{22}y + t_y + \sum_i c_i g(\|\mathbf{x} - p_i\|)}. \quad (7)$$

where  $\mathbf{x}$  are the control points in both images and  $g(\cdot)$  is the actual radial basis function.

Two radial basis functions have been used: (i) the thin plate spline (TPS) and (ii) the B-splines. Apart from the formalism, these two approaches have a main difference. With B-splines, the control points are usually uniformly and densely placed on a grid where as with TPS, the control points correspond to detected or selected key points. By using TPS, [129] obtained more accurate and time efficient results than with the B-splines strategy ([128]).

It is reasonable to point out that usually only rigid or affine registrations have been used to register multi-parametric images from a same protocol. Elastic registration methods are more commonly used to register multi-protocol images (e.g., histopathology with MRI images) ([196, 197]).

### 3.3.2. Similarity measure

During the registration procedure, a similarity criterion is computed in order to evaluate the quality of the alignment performed. Roughly speaking, this criterion will give the direction to take to the optimizer, in order to assign the most optimal values to the geometric transformation parameters.

The most naive similarity measure is the mean squared error (MSE) of the SI of MRI images. However, this metric is not well suited when multi-parametric images are involved due to the tissue appearance variations between the different modalities.

In that regard, MI was introduced as a registration measure in the late 1990's by [155]. The MI measure finds its foundation in the assumption that a homogeneous region in the first modality image should also appear as a homogeneous region in the second modality even if their SIs are not identical. Thus, those regions share information and the registration task can be achieved by maximizing this common information. Maximizing the MI is in fact equivalent to minimizing the joint entropy which is a measure related with the degree of uncertainty or dispersion of the data in the joint histogram. As shown in Fig. 10, the data in the joint histogram will be concentrated in the case of aligned images while will be more randomly distributed in the case of misaligned images.

A generalized form of MI, CMI, was proposed by [30]. CMI encompasses interdependent information such as texture and gradient into the metric.

### 3.3.3. Optimization methods

Registration is usually regarded as an optimization problem where the parameters of the geometric transformation model have to be inferred by minimizing the similarity measure. Iterative estimation methods are commonly used: L-BFGS-B quasi-Newton method ([25]) and gradient descent ([205]). During our review, we noticed that authors do not usually linger over optimizer choice.

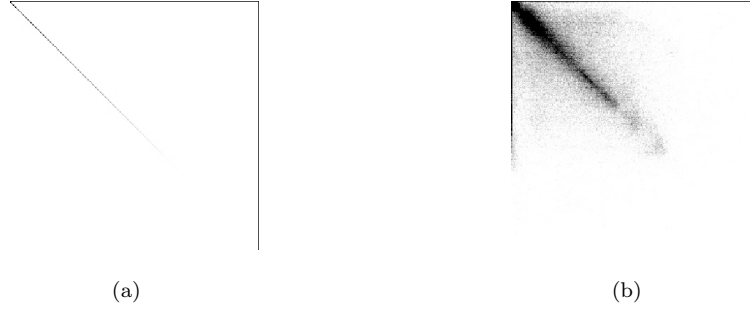


Figure 10: Difference observed in joint histogram between aligned (Fig. 10(a)) and misaligned (Fig. 10(b)) images.

#### 3.3.4. Interpolation

The registration procedure involves transforming an image, and pixels mapped to non-integer points must be approximated using interpolation methods. As for the optimization methods, we notice that little attention has been paid on the choice of those interpolations methods. However, commonly used methods are bilinear, nearest-neighbour, bi-cubic, spline and inverse-distance weighting method ([127]).

#### 3.3.5. Review of the methods used in CAD system

Studies presenting a CAD pipeline incorporating an automatic registration procedure are summarized in Tab. 5.

[7, 8] did not use the framework as presented in Fig. 9 to register 2D T<sub>2</sub>-W and DCE images. By using image symmetries and the MSE metric, they found the parameters of an affine transformation but without using a common objective function. They were finding independently and consecutively the scale factor, the rotation and finally the translation.

[59] used also a in-house development registration method to register 2D T<sub>2</sub>-W and DW images using an affine model. The bladder is first segmented in both modalities in order to obtain its contours and to focus the registration.

[59] and also [213] used the same framework ([167]) which is based on finding an affine transformation to register the T<sub>2</sub>-W and DCE images using MI. Then, an elastic registration using B-spline takes place using the affine parameters to initialize the geometric model with the same similarity measure. However, the approaches differ regarding the choice of the optimizer since [59] used a gradient descent and [213] tackle the optimization via a quasi-Newton method. Moreover, [59] performed a 2D registration whereas [213] registered 3D volumes.

[207, 208] as well as [212] performed an affine registration using the MI as similarity measure to correct the misalignment between T<sub>2</sub>-W and DCE images. The choice of the optimizer was not specified. [207, 208] focused on 2D registration while [212] performed 3D registration.

Finally, [206] performed a 3D registration with the three modalities, T<sub>2</sub>-W and DCE and DW MRI,

Table 6: Overview of the CADe strategies employed in CAD systems.

CADe: ROIs selection strategy	References
All voxels-based approach	[4-5,7-8,13,15,17-18,21-23,26-38]
Lesions candidate detection	[10-12,42]

by using an affine transformation model combined with the CMI similarity measure as presented in [30]. Moreover, [30] employed gradient descent to solve this problem but suggested Nelder-Mead simplex and quasi-Newton method as other solutions.

#### 4. CADe - CADx

##### 4.1. CADe: ROIs detection/selection

As discussed in the introduction and shown in Fig. 1, the image classification framework is composed of eventually a CADe and a CADx. In this section, we will focus on studies embedding a CADe in their framework. Two approaches are considered to define a CADe (see Tab. 6): (i) voxel-based delineation and (ii) lesion segmentation.

The first strategy, which concerns the majority of the studies reviewed (see Tab. 6), is in fact linked to the nature of the classification framework. All voxels are considered as a possible lesion and the output of the framework will be pixels classified as lesion and non lesion.

The secondary group of methods is composed of method implementing a lesion segmentation algorithm to delineate potential candidates to further obtain a diagnosis through the CADx. This approach was borrowed from methodologies applied successfully in CADe such as for breast cancers. These methods are in fact very similar to the classification framework used in CADx later.

[211] highlighted lesion candidates by detecting blobs in the ADC map. These candidates were filtered using some *a priori* criteria such as SI or diameter. The candidate blobs detected are then filtered depending on their appearances (cf. maximum of the likelihood of the region, diameter of the lesion) and their SI in ADC and T<sub>2</sub>-W images. The detected regions are then used as inputs for the CADx.

[109] used a pattern recognition approach in order to delineate the ROIs. A blobness map was calculated in the same manner as previously in [213] using the multi-resolution Hessian blob detector on the ADC map, T<sub>2</sub>-W and pharmacokinetic parameters maps (see Sect. 4.2 for details about those parameters). Additionally, the position of the voxel  $\mathbf{x} = \{x, y, z\}$  was used as a feature as well as the Euclidean distance of the voxel to the prostate center. Hence, the feature vectors were composed of eight features and a support

vector machines (SVM) classifier was trained using a radial basis function (RBF) kernel (see Sect. 4.4 for more details).

Subsequently, [108] modified this approach by including only features related to the blob detection on the different maps as well as the original SIs of the parametric images. Two new maps were introduced based on texture. Instead of a SVM classifier, a  $k$ -nearest neighbour ( $k$ -NN) classifier was used. The candidate regions were then extracted by performing a local maxima detection followed by post-processing region-growing and morphological operations.

In a similar way, [105] used the same approach and add two new features: (i) a Gaussian texture bank on  $T_2$ -W to create new maps and (ii) the DW MRI image acquired with  $b = 800 \text{ s.mm}^{-2}$  was included too. Three classifiers were tested: (i) linear discriminant analysis (LDA), (ii) GentleBoost and (iii) Random forest. After evaluation, random forest was selected as classifier due to its overall performances.

#### 4.2. CADx: Feature detection

Discriminative features which can be used to recognize CaP from healthy tissue have to be first detected. This processing is known in computer vision as feature extraction. However, feature extraction is also the name given in pattern recognition to some types of dimension reduction methods which will be presented in the next section. In order to avoid confusion between these two aspects, in this survey, the procedure “detecting” or “extracting” features from images and signals will be defined as feature detection. This section will summarize the different strategies employed for this task. The features used in the studies reviewed are summarized in Tab. 7.

Table 7: Overview of the feature detection methods used in CAD systems.

Feature detection methods	Indexes
<b>MRI image:</b>	
<i>Voxel-wise detection</i>	
Intensity-based	✓- - [1-2,39] - - ✓ [7] ✓- ✓ [4-6,9-13,21-22] ✓✓✓ [19-20]
Edge-based	✓- - [30-31,33-34]
Prewitt operator	✓- - [30-31,33-34,36-38]
Sobel operator	✓✓✓ [19-20]
Kirsch operator	✓- - [30-31,33-34,36-38] ✓✓✓ [19-20]
Gabor filtering	✓- - [32,34,38]
Texture-based	✓- - [3,30-31,33-34,36,38]
Haralick features	✓✓- [37] ✓✓✓ [11,19-20] ✓- - [15-16] ✓✓✓ [19-20] ✓- - [38] ✓- - [12] [6,10-12]
Fractal analysis	
Discrete cosine transform (DCT)	
Wavelet-based features	
Gaussian filter bank	
Position-based	
<i>Region-wise detection</i>	
Statistical-based	- ✓- [40]
Percentiles	- - ✓ [3,24] ✓✓- [41] ✓✓✓ [10-12,19-20,42] ✓- - [1-2,30-31,33-34,36,38] - - ✓ [3] ✓✓- [37] ✓- ✓ [24] ✓✓✓ [10-12,19-20]
Statistical-moments	✓✓✓ [14] ✓✓✓ [14] ✓✓✓ [14] ✓✓✓ [14] [11-12,16]
Histogram-based	
PDF	
HOG	
Shape context	
LBP	
Anatomical-based	
<b>DCE signal:</b>	
Whole spectra approach	[1,2]
Semi-quantitative approach	✓ <sup>†</sup> [25] [18-20,26]
Quantitative approach	✓ <sup>†</sup> [14,25]
Toft model	[7,9-12,18-20]
Brix model	✓ <sup>†</sup> [4-5,21-22] [13,26] [7,18] [7,18]
Weibull function	
PUM	
<b>MRSI signal:</b>	
Whole spectra approach	[8,17,23,27-31,33-34]
Quantification approach	[8,23]
Wavelet-based approach	[32]

Notes:

( ✓/- ✓/- ✓/- ): triplet stating of the implementation or not of the feature for respectively T<sub>2</sub>-W-MRI images, DCE-MRI images, DW-MRI images.

✓: used or implemented.

✓<sup>†</sup>: partially implemented.

Table 8: Parameters used as features for a DCE semi-quantitative analysis in CAD systems.

Semi-quantitative features	Explanations
<i>Amplitude features:</i>	
$S_0$	Amplitude at the onset of the enhancement
$S_{\max}$	Amplitude corresponding to 95% of the maximum amplitude
$S_p$	Amplitude corresponding to the maximum amplitude
$S_f$	Amplitude at the final time point
<i>Time features:</i>	
$t_0$	Time at the onset of the enhancement
$t_{\max}$	Time corresponding to 95% of the maximum amplitude
$t_p$	Time corresponding to the maximum amplitude
$t_f$	Final time
$t_{tp}$	Time to peak which is the time from $t_0$ to $t_p$
<i>Derivatives and integral features:</i>	
$WI$	Wash-in rate corresponding to the signal slope from $t_0$ to $t_m$ or $t_p$
$WO$	Wash-out rate corresponding to the signal slope from $t_m$ or $t_p$ to $t_p$
$IAUC$	Initial area under the curve which is the area between $t_0$ to $t_f$

#### 4.2.1. Image-based features

This section will focus on image-based features detection. Two main strategies to detect features have been identified and used for the purpose of our classification: (i) voxel-wise detection and (ii) region-wise detection.

- **Voxel-wise features:** This strategy refers to the fact that a feature is extracted at each voxel location of an image.

CaP as previously discussed (see Tab. 2.2.2) can be discerned due to SI changes. Hence, intensity-based features are one of the most common features used to build the feature vector which has to be classified ([7, 8, 12, 13, 29, 94, 105, 108, 109, 112, 133, 134, 206, 207]). This type of feature consists simply of the SI of each voxel of the different MRI modalities.

SI changes can be viewed as heterogeneous regions and edge-based features are used in that regard. Each feature is computed by convolving the original image with an edge operator. Three of these operators are used in CAD systems: (i) Prewitt operator ([156]), (ii) Sobel operator ([177]) and (iii) Kirsch operator ([90]). Results obtained with these operators vary, due to their different kernels. These features are commonly incorporated in the feature vector for further classification in the CAD systems reviewed ([133, 134, 187, 188, 192, 206, 209]).

Gabor filters ([42, 57]) offer another approach to extract information related to edges and texture.

[207, 210] and [193] integrated Gabor analysis in their feature vector.

Texture-based features provide other characteristics discerning CaP from healthy tissue. The most common texture analysis for image classification are co-occurrence matrices with their related statistics which were proposed by [71] and are commonly used in CAD systems ([11, 133, 134, 187, 188, 192, 206, 207, 209, 210]).

Fractal analysis and more precisely a local estimation of the fractal dimension ([18]) describing the texture roughness at a specific location was used in [113]. A wavelet-based method in a multi-resolution framework was used to estimate the fractal dimension. Cancerous tissue were characterized to have a higher fractal dimension than healthy tissue.

[29] aimed to describe the texture using the frequency signature via the discrete cosine transform (DCT) ([2]) defining a neighbourhood of  $7 \times 7$  pixels for each of the modalities that they used.

In the same spirit, [210] projected T<sub>2</sub>-W images into the wavelet space and used the coefficients obtained from the decomposition as features. The wavelet family used for the decomposition was the Haar wavelet.

[105] compute texture map based on T<sub>2</sub>-W images using a Gaussian filter bank ([99]).

The position of a voxel within the prostate was also considered a possible feature. [105, 109] computed the Euclidean distance from each voxel to the prostate center as well as the individual distance in the three directions  $x$ ,  $y$  and  $z$ . [29] embedded the same information but this time using cylindrical coordinates  $r$ ,  $\theta$  and  $z$  corresponding to the radius, azimuth and elevation respectively.

– ***Region-wise features:***

Unlike the previous section, another strategy is to study an entire region and extract characteristic features corresponding to this region.

The most common approach reviewed can be classified as statistical methods. First, a feature map are computed for the whole image and not any more for a single voxel. Then, ROIs are defined and statistics are extracted from each of these regions. The first type of statistic is based on percentiles and is widely used ([11, 105, 108, 109, 150, 187, 188, 192, 206, 207, 209–214]). In fact, once that a ROI is defined, the features corresponding to the  $n^{\text{th}}$  percentile are used as feature. This  $n$  can take any value between 0 and 100. This threshold is usually manually determined observing the distribution and corresponds to the best discriminant value differentiating malignant and healthy tissue. In addition, statistic-moments such as mean, standard deviation, kurtosis and skewness are also used ([7, 8, 11, 133, 134, 150]). [105] also introduced a feature based on symmetry. They compute the mean of a candidate lesion as well as its mirrored counter-part and compute the quotient as feature.

Another subset of features are anatomic which were also used by [105, 108] and [122]. [105, 108] computed the volume, compactness and sphericity related to the region to integrate it in their feature



vector to later classify. [122] introduced four features corresponding to the percentage of tissue belonging to the regions PZ, CG, periurethral region or outside prostate region for the considered ROI.

In contrast to anatomical are histogram-based feature descriptors. For instance, [110] introduced four different types of histogram-based features. The first type corresponds to the histogram of the SI of the image. The second type is the histogram of oriented gradient (HOG) ([41]). HOG descriptor describes the local shape of the object of interest by using gradient directions distribution. The third histogram-based type used by [110] was shape context ([17]). The shape context is also a way to describe the shape of an object of interest. The last set of histogram-based feature extracted is based on the framework of [221] which is using the Fourier transform of the histogram created via local binary pattern (LBP) ([140]).

The last group of region-based feature is based on fractal analysis. The features proposed are based on estimating the fractal dimension which is a statistical index representing the complexity of what is analysed. [115] proposed two features based on fractal dimension: (i) texture fractal dimension and (ii) histogram fractal dimension. [113] proposed a 3D version to estimate the fractal dimension of a volume using wavelet decomposition.

#### 4.2.2. DCE-based features

DCE-MRI is more commonly based on a SI analysis over time as presented in Sect. 2.2.2. The parameters extracted used in CAD system during the DCE-MRI analysis are presented.

- **Whole-spectra approach:** Some studies are using the whole DCE time series as feature vector such as [7, 8], [193] and [207, 209]. In some cases, the high-dimensional feature space is reduced using dimension reduction methods as it will be presented in the next section (see Sect. 4.3).
- **Semi-quantitative approach:** Semi-quantitative approaches are based on mathematically modelling the DCE time series. The parameters modelling the signal are commonly used mainly due to the simplicity of their computation. Parameters included in semi-quantitative analysis are summarized in Tab. 8 and also graphically depicted in Fig. 11. A set of time features corresponding to specific amplitude level (start, maximum and end) are extracted. Then, derivative and integral features are also considered as discriminative and are commonly computed.
- **Quantitative approach:** As presented in Sect. 2.2.2, quantitative approaches correspond to mathematical-pharmacokinetic models based on physiological exchanges. Four different models have been used in CAD systems. The most common model reviewed was the Brix model using three parameters  $A$ ,  $k_{ep}$  and  $k_{el}$  ([12, 13, 112, 143, 144, 183]). The Tofts model and more precisely the parameters  $K_{trans}$ ,  $k_{ep}$  and  $v_e$  ([195]) was used by [59, 94, 105, 108, 109, 123, 133, 134].

[123] and [59] used the Weibull function defined by two parameters. They also used another empirical model which is based on the West-like function and named the phenomenological universalities model

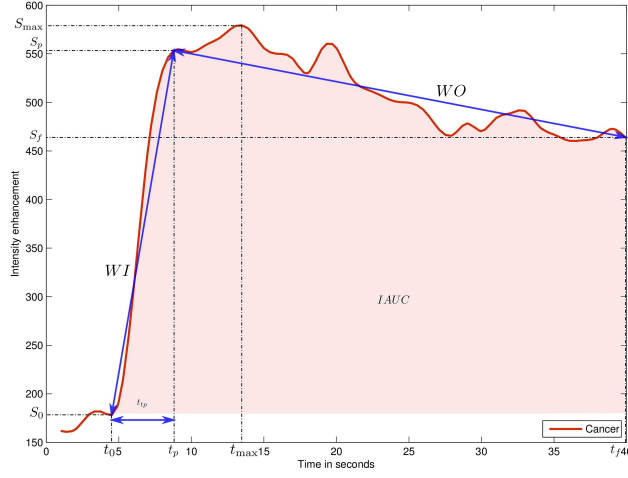


Figure 11: Graphical representation of the different semi-quantitative features used for DCE-MRI analysis.

([27]) using the three parameters the parameters  $\beta$ ,  $a_0$  and  $r$ .

For all these models, the parameters are inferred using an optimization curve fitting approach.

#### 4.2.3. MRSI-based features

- **Whole spectra approach:** As in the case of DCE analysis, one common approach is to incorporate the whole MRSI spectra in the feature vector for classification ([87, 122, 148, 187–189, 191, 192, 207]). Sometimes post-processing involving dimension reduction methods is performed to reduce the complexity during the classification as it will be presented in Sect. 4.3.
- **Quantification approach:** We can reiterate that in MRSI only few biological markers (cf., choline, creatine and citrate metabolites mainly) are known to be useful to discriminate CaP and healthy tissue. Then, concentrations of these metabolites can be considered as a feature used for classification. In order to perform this quantification, four different approaches have been used. The QUEST ([162]), AMARES ([200]) and VARPRO ([37]) models were used by [87]. They are all time-domain quantification methods varying by the type of pre-knowledge embedded and the optimization approaches used to solve the quantification problem. Unlike the time-domain quantification approaches, [148] used the LcModel approach ([157]) which solves the optimization problem in the frequency domain.

Once the different concentrations are computed, [87] calculated the relative concentrations (Eq. (8) and (9)) and used them as features. However, [148] used each metabolite concentrations individually.

$$R_1 = \frac{[\text{Cho}] + [\text{Cr}]}{[\text{Cit}]} . \quad (8)$$

$$R_2 = \frac{[\text{Cit}]}{[\text{Cho}] + [\text{Cr}] + [\text{Cit}]} , \quad (9)$$

where Cit, Cho and Cr are the concentration of citrate, choline and creatine respectively.

- **Wavelet decomposition approach:** [193] performed a wavelet packet decomposition ([36]) with the Haar wavelet basis function and used the coefficients of this decomposition as features for further classification.

#### 4.3. CADx: Feature selection and feature extraction

As presented in the previous section, a wide variety of features can be computed (see Tab. 7). This often leads from multi-parametric MRI data to a high dimensions feature space which might mislead or corrupt the classifier used for training. Thus, it is often of interest to reduce the number of dimensions before proceeding to the classification task. The strategies used can be grouped as: (i) feature selection and (ii) feature extraction and those methods will be presented in the above sections. However, only the methods used in CAD system are presented and summarized in Tab. 9.

##### 4.3.1. Feature selection

The feature selection strategy is based on selecting the most discriminative feature dimensions of the high-dimensional space. Thus, the low-dimensional space is then composed of a subset of the original features detected. In this section, methods employed in the studies reviewed will be briefly presented. More extensive reviews specific to feature selection can be found in [168].

[133, 134] make use of the p-value by using the independent two-sample t-test with equal mean for each feature dimension. The features can be ranked and the most significant features can be selected. However, this technique suffers from a main drawback since it assumes that each feature is independent, which is unlikely to happen and introduces a high degree of redundancy in the features selected.

[211] employed a similar feature ranking approach but make use of the Fisher discriminant ratio to compute the relevance of each feature dimension. Once the features are ordered, [211] select the feature dimensions with the larger Fisher discriminant ratio.

MI can also be used to select a subset of feature dimensions. [149] introduced two main criteria to select the feature dimensions: (i) maximal relevance and (ii) minimum redundancy. Combination of these two criteria is known as minimum redundancy maximum relevance (mRMR)<sup>4</sup> ([149]) and are computed as a difference or quotient. [133, 134] make use of maximal relevance criterion alone and also of both mRMR difference and quotient criterion. [210] also reduced their feature vector via mRMR difference and quotient.

---

<sup>4</sup>mRMR implementation can be found at: <http://penglab.janelia.org/proj/mRMR/>

Table 9: Overview of the feature selection and extraction methods used in CAD systems.

Dimension reduction methods	References
<i>Feature selection:</i>	
Statistical test	[19-20,42]
MI-based methods	[19-20,38]
<i>Feature extraction:</i>	
Linear mapping	
PCA	[28-29,32]
Non-linear mapping	
Laplacian eigenmaps	[27,29-31,34,37]
LLE and LLE-based	[28-29,34-35]

#### 4.3.2. Feature extraction

The feature extraction strategy is related to dimension reduction methods but not selecting discriminative features. Instead, these methods aim at mapping the data from the high-dimensional space into a low-dimensional space created to maximize the separability between the classes. The mapping can be performed in a linear or a non-linear manner. Again, only methods employed in CAD system will be reviewed in this section. We refer the reader to the review of [51] for a full review of feature extraction techniques.

PCA is the most commonly used linear mapping method in CAD prostate ([84]). [190, 191, 193] used PCA in order to reduce the dimensionality of their feature vector.

Non-linear mapping was also used for dimension reduction. It is mainly based on Laplacian eigenmaps and locally linear embedding (LLE) methods. Laplacian eigenmaps<sup>5</sup>, also referred as spectral clustering in computer vision, aim to find a low-dimensional space in which the proximity of the data should be preserved from the high-dimensional space ([16, 174]). [189, 191, 192, 209] used this spectral clustering to project their feature vector into a low-dimensional space. The feature space in these studies is usually composed of features extracted from a single or multiple modalities and then concatenated before applying the Laplacian eigenmaps dimension reduction technique.

[187, 191] used a slightly different approach by combining the Laplacian eigenmaps techniques with a prior multi-kernel learning strategy.

LLE<sup>6</sup> is another common non-linear dimension reduction technique widely used, first proposed by [166]. [190] used a modified version of the LLE algorithm in which they applied LLE in a bagging approach with multiple neighbourhood sizes. The different embeddings obtained are then fused using the maximum

<sup>5</sup>Laplacian eigenmap implementation is available at: <http://www.cse.ohio-state.edu/~mbelkin/algorithms/algorithms.html>

<sup>6</sup>LLE implementation is available at: <http://www.cs.nyu.edu/~roweis/lle/code.html>

likelihood (ML) estimation.

#### 4.4. CADx: Classification

##### 4.4.1. Classifier

Once the feature vector has been extracted and eventually the complexity reduced, it is possible to make a decision and classify this feature vector to belong to CaP or healthy tissue. Classification methods used in a CAD system to distinguish these two classes are summarized in Tab. 10. A full review of classification methods used in pattern recognition can be found in [19].

##### – *Rule-based method:*

[115] make use of a decision stump classifier to distinguish CaP and healthy classes.

[158] detect CaP by implementing a given set of rules using a score scheme in a medical decision making approach. The feature values are compared with a pre-defined threshold. Then, at each comparison, the final score is incremented or not, depending on the threshold and the final decision is taken depending of the final score.

##### – *Clustering methods:*

$k$ -nearest neighbour ( $k$ -NN) is one of the simplest supervised machine learning classification methods.  $k$ -NN was one of the methods used by [133, 134] mainly to make a comparison with different machine learning techniques. [108] used this method to roughly detect potential CaP voxels before performing a region-based classification.

$k$ -means is an unsupervised clustering method in which the data have to be partitioned into  $k$  clusters. The discovery of the clusters is an iterative procedure. This algorithm can also be used for “on-line” learning. In case that new data has to be incorporated, the initial centroid positions correspond to the results of a previous  $k$ -means training and is followed by the assignment-updating stage previously explained.

[189, 191] used  $k$ -means in an iterative procedure. Three clusters were defined corresponding to CaP, healthy and non-prostate, respectively.  $k$ -means was applied iteratively and the voxels corresponding to the largest cluster were excluded under the assumption that it is assigned to “non-prostate” cluster. The iteration stop when the number of voxels composing all clusters remaining is smaller than a threshold.

[190, 207, 209] used  $k$ -means in a repetitive manner to be less sensitive to the centroids initialisation. Thus,  $k$  clusters were generated  $T$  times. The final assignment was performed by majority voting using a co-association matrix as proposed by [52].

##### – *Linear model classifiers:*

Linear discriminant analysis (LDA) can be used as a classification method in which the optimal linear separation between two classes is found by maximizing the interclass variance and minimizing the

Table 10: Overview of the classifiers used in CAD systems.

Classifier	References
<i>Rule-based method:</i>	[16,25]
<i>Clustering methods:</i>	
<i>k</i> -means clustering	[27-29,34-35]
<i>k</i> -NN	[11,19-20]
<i>Linear model classifiers:</i>	
LDA	[3,6,12,19-20,42]
Logistic regression	[8-9]
<i>Non-linear classifier:</i>	
QDA	[38]
<i>Probabilistic classifier:</i>	
Naive Bayes	[7,18-20]
<i>Ensemble learning classifiers:</i>	
AdaBoost	[12,15]
Random forest	[8,12,32-33,36]
Probabilistic boosting tree	[30-32,37]
<i>Kernel method:</i>	
Gaussian processes	[8]
<i>Sparse kernel methods:</i>	
SVM	[4-6,8,10-11,14-15,19-24,26,32,39-41]
RVM	[21-22]
<i>Neural network:</i>	
Multiple layer perceptron	[17,23]
Probabilistic neural network	[1-2,37]
<i>Graphical model classifiers:</i>	
Markov random field	[13,22]
Conditional random field	[4-5]

intra-class variance ([55]). [11, 29, 105, 133, 134, 211] used LDA to classify their feature vectors defining two classes CaP *versus* healthy.

Logistic regression can be used to perform binary classification and can provide the probability of an observation to belong to a class. [87, 158] used a logistic regression to create a linear probabilistic model in order to classify their feature vectors.

– ***Non-linear model classifier:***

[210] used the most general quadratic discriminant analysis (QDA) instead of LDA. Unlike in LDA in which one assumes that the class covariance matrix  $\Sigma$  is identical for all the classes, in QDA, a covariance matrix  $\Sigma_k$  specific to each class is computed.

– ***Probabilistic classifier:***

The most commonly used classifier is the naive Bayes classifier which is a probabilistic classifier assuming independence between each feature dimension ([163]). [59, 123, 133, 134] used the naive Bayes classifier to classify their feature vectors as either malignant or healthy. The Normal distribution was used as the likelihood probability for that model.

– ***Ensemble learning classifiers:***

AdaBoost is an adaptive method based on an ensemble learning method and was initially proposed by [54]. AdaBoost linearly combines several weak learners resulting into a final strong classifier. A weak learner is defined as a classification method performing slightly better than random classification. Random forest<sup>7</sup> is a classification method which is based on creating an ensemble of decision trees and was introduced by [22]. Probabilistic boosting-tree is another ensemble learning classifier which shares principles with AdaBoost but using them inside a decision tree ([198]).

[113] make use of the AdaBoost classifier to perform their classification while [105] used the GentleBoost variant ([56]) which provides a modification of the function affecting the weight at each weak classifier. [87, 105, 187, 193, 208] focused on the random forest classifier whereas [188, 192, 193, 206] performed their classification using the probabilistic boosting-tree classifier.

– ***Kernel method:***

A Gaussian process<sup>8</sup> for classification is a kernel method in which it is assumed that the data can be represented by a single sample from a multivariate Gaussian distribution ([161]). Only the work of [87] used a Gaussian process for classification in order to distinguish CaP in MRSI data.

– ***Sparse kernel methods:***

---

<sup>7</sup>Random forest implementation can be found at: [http://www.stat.berkeley.edu/~breiman/RandomForests/cc\\_software.htm](http://www.stat.berkeley.edu/~breiman/RandomForests/cc_software.htm)

<sup>8</sup>Gaussian process implementation can be found at: <http://www.gaussianprocess.org/gpml/code/matlab/doc/index.html>

In a classification scheme using Gaussian processes, when a prediction has to be performed, the whole training data will be used to assign a label to the new observations. That is why this method is also called kernel method. Sparse kernel category is composed of methods which rely only on a few labelled observations of the training set to assign the label of new observations ([19]).

Support vector machines (SVM)<sup>9</sup> is a sparse kernel method which aims at finding the best linear hyperplane (non-linear separation is discussed further) which separates two classes such that the margin between the two classes is maximized ([201]).

SVM can also be used as a non-linear classifier by performing a kernel trick ([20]). The original data  $\mathbf{x}$  can be projected to a higher-dimension space in which it is assumed that a linear hyperplane will better split the classes. Different kernels are popular such as the RBF kernel, polynomial kernels or Gaussian kernel.

In prostate CAD system, SVM is the most popular classification method and was used in a multitude of research works: [12, 13, 29, 87, 108–110, 113, 133, 134, 143, 144, 148, 150, 183, 193, 211–214].

Relevant vector machine (RVM) is a sparse version of Gaussian process previously presented and was proposed by [186]. RVM is identical to a Gaussian process with the following covariance function ([159]):

$$K_{RVM}(\mathbf{x}_p, \mathbf{x}_q) = \sum_{j=1}^M \frac{1}{\alpha_j} \Phi_j(\mathbf{x}_p) \Phi_j(\mathbf{x}_q) , \quad (10)$$

where  $\phi(\cdot)$  is a Gaussian basis function,  $\mathbf{x}_i | i = \{1, \dots, N\}$  are the  $N$  training points and  $\boldsymbol{\alpha}$  are the weights vector.

As mentioned in [159], the sparsity regarding the relevance vector arises if  $j\alpha_j^{-1} = 0$ . The set of weights  $\boldsymbol{\alpha}$  is inferred using the expectation maximization algorithm. [143, 144] make use of RVM and make a comparison with SVM for the task of CaP detection.

#### – *Neural network:*

Multilayer perceptron is a feed-forward neural networks considered as the most successful model of this kind in pattern recognition ([19]). The most well known model used is based on two layers. [122, 148] used this classifier to classify MRSI spectra.

Probabilistic neural networks are another type of feed-forward networks which can be derived from the multilayer perceptron case and was proposed by [178]. This classifier can be modelled by changing the activation function of the hidden layer to an exponential function. This method was used by [7, 8, 206] in order to perform the classification of their multi-parametric features vector.

#### – *Graphical model classifiers:*

---

<sup>9</sup>SVM implementation can be found at: <http://www.csie.ntu.edu.tw/~cjlin/libsvm/>



Table 11: Overview of the model validation techniques used in CAD systems.

Model validation techniques	References
LOOCV	[1-8,11,18-22,24,25,33,37,39-41]
$k$ -CV	[10,23,29-33,38,36,42]

Markov random fields can also be used for classification in order to perform a lesion segmentation method to detect CaP. [112, 144] used Markov random fields as an unsupervised method to segment lesions in multi-parametric MRI images.

[12, 13] used conditional random fields instead of Markov random fields to segment their MRI images.

#### 4.4.2. Model validation

In pattern recognition, the use of model validation techniques to assess the performance of trained classifiers is quite important. Two techniques are broadly used in the development of CAD system and are summarized in Tab. 11.

The most popular technique used in CAD systems (see Tab. 11) is the leave-one-out cross-validation (LOOCV) technique. From the whole data, one patient is kept for validation and the other cases are used to train. This manipulation is repeated until each patient has been used for validation. This technique is popular when working with medical data due to the restricted number of patients included in datasets. Thus, it allows us to train on a fair number of patients even with a small dataset. However, this technique suffers from high variance and can be considered as an unreliable estimate ([48]).

The other very well known technique used for assessing classifiers is the  $k$ -fold cross-validation ( $k$ -CV) technique. This technique is based on splitting the dataset into  $k$  subsets where the samples are randomly selected. Then, one fold is kept for the validation and the remaining subsets for training. The classification is then repeated as in the LOOCV technique. In our review, the typical values used for  $k$  were set to three and five. This technique is more appropriate than the previous one since it does not suffer from large variance. However, the number of patients in the dataset needs to be large enough for the results to be meaningful.

#### 4.4.3. Evaluation measure

Several metrics can be used in order to assess the performance of the classifier trained when tested on the test data. The techniques used for evaluation of the CAD system for CaP detection are summarized in Tab. 12.

Using the classification approach previously presented, each voxel in the MRI image will be classified.

Table 12: Overview of the evaluation metrics used in CAD systems.

Evaluation metrics	References
Accuracy	[4-5,13,26,32]
Sensitivity - Specificity	[4-5,7,13,15,18,21-24,26,28-29,34-35]
ROC - AUC	[2-3,6-9,14-20,24,30-33,36-41]
FROC	[10-11,42]
Dice's coefficient	[4-5,13,21]

Comparison with a ground-truth can give rise to a confusion matrix by counting true positive, true negative, false positive and false negative samples. From this analysis, different statistics can be extracted.

The first statistic used is the accuracy which is computed as the ratio of true detection to the number of samples. However, depending on the strategy employed in the CAD work-flow, this statistic can be highly biased by a high number of true negative samples which will boost the accuracy score and does not represent the actual performance of the classifier.

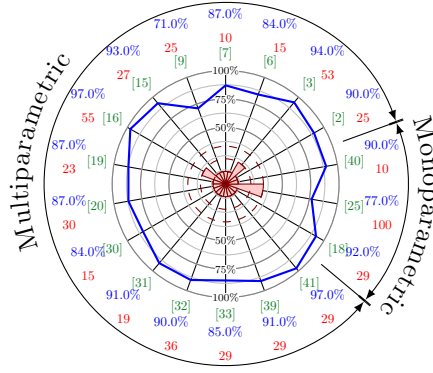
That is why, the most common statistic computed are sensitivity and specificity which give a full overview of the performance of the classifier trained. Sensitivity is also called the true positive rate and is equal to the ratio of the true positive samples over the true positive added with the false negative samples as shown in Eq. (11). Specificity is also named the true negative rate and is equal to the ratio of the true negative samples over the true negative added with the false positive samples as shown in Eq. (12).

$$SEN = \frac{TP}{TP + FN} , \quad (11)$$

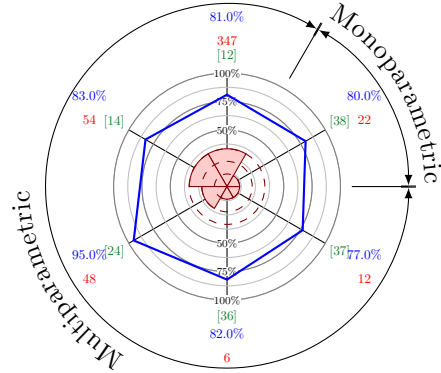
$$SPE = \frac{TN}{TN + FP} . \quad (12)$$

These statistics can be used to compute the receiver operating characteristic (ROC) curves ([125]). This analysis represents graphically the sensitivity as a function of (1 - specificity), which is in fact the false positive rate, by varying the discriminative threshold of the classifier. By varying this threshold, more true negative samples will be found but often at the cost of detecting more false negatives. However, this fact is interesting in CAD since it is possible to obtain a high sensitivity and to ensure that no cancers are missed even if more false alarms have to be investigated. A statistic derived from ROC analysis is the area under the curve (AUC) which corresponds to the area under the ROC and is a measure used to make comparisons between models.

The ROC analysis can be classified as a pixel-based evaluation method. However, a cancer can be



(a) Comparison in terms of AUC-ROC of the methods using data from 1.5 Tesla MRI scanner.



(b) Comparison in terms of AUC-ROC of the methods using data from 3.0 Tesla MRI scanner.

Figure 12: Comparison of the results in terms of AUC for 1.5 and 3.0 Tesla MRI scanners. The blue value represents the metric and are graphically reported in the blue curve in the center of the figure. The red value and areas correspond to the number of patients in the dataset. The numbers between brackets in green correspond to the reference as reported in Tab. 2.

also considered as a region. The free-response receiver operating characteristic (FROC) extends the ROC analysis but to a region-based level. The same confusion matrix can be computed were the sample are not pixels any more but refer to a lesion. However, it is important to define what is a true positive sample in that case. Usually, a lesion is considered as a true positive sample if the region detected by the classifier overlaps “sufficiently” the one delineated in the ground-truth. However, “Sufficiently” is a subjective measure defined by each researcher and can correspond to one pixel only. However, an overlap of 30 to 50 % is usually considered.

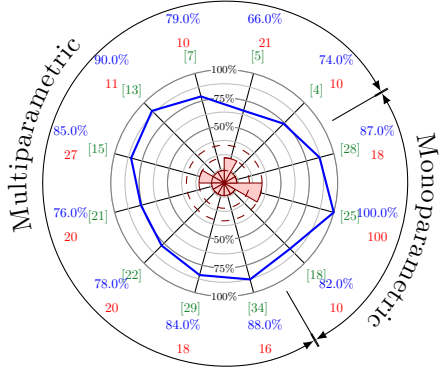
Finally, to evaluate the accuracy of the lesion localization, the Dice’s coefficient is sometimes computed which corresponds to the similarity between a detected lesion and its ground-truth. This coefficient consists of the ratio of twice the number of pixels in common to the sum of the pixels of the lesions in the ground-truth  $GT$  and the output of the classifier  $S$  defined as shown in Eq. (13).

$$Q_D = \frac{2|GT \cap S|}{|GT| + |S|}. \quad (13)$$

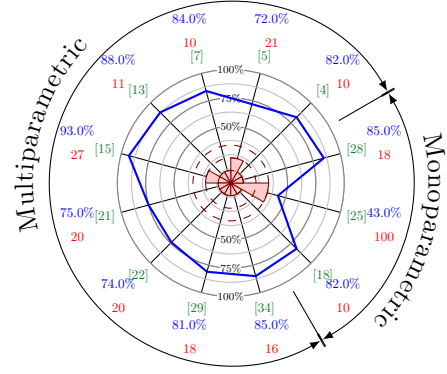
## 5. Discussion

### 5.1. Results reported

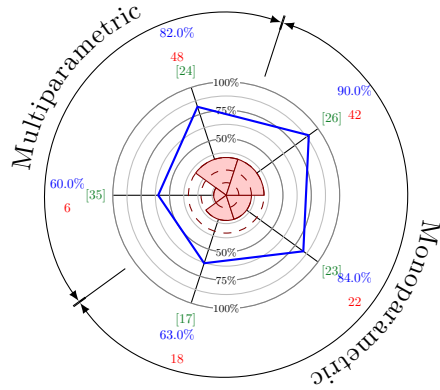
As discussed previously in Sect. 4.4.3, different metrics have been used to report results. A comparison of the different methods reviewed is given depending on the metric used in field of research and also the



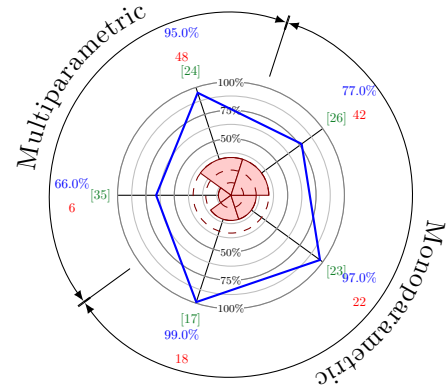
(a) Comparison in terms of sensitivity of the methods using data from 1.5 Tesla MRI scanner.



(b) Comparison in terms of specificity of the methods using data from 1.5 Tesla MRI scanner.



(c) Comparison in terms of sensitivity of the methods using data from 3.0 Tesla MRI scanner.



(d) Comparison in terms of specificity of the methods using data from 3.0 Tesla MRI scanner.

Figure 13: Comparison of the results in terms of sensitivity (13(a),13(c)) and specificity (13(b),13(d)) for 1.5 and 3.0 Tesla MRI scanners. The blue value represents the metric and are graphically reported in the blue curve in the center of the figure. The red value and areas correspond to the number of patients in the dataset. The numbers between brackets in green correspond to the reference as reported in Tab. 2.

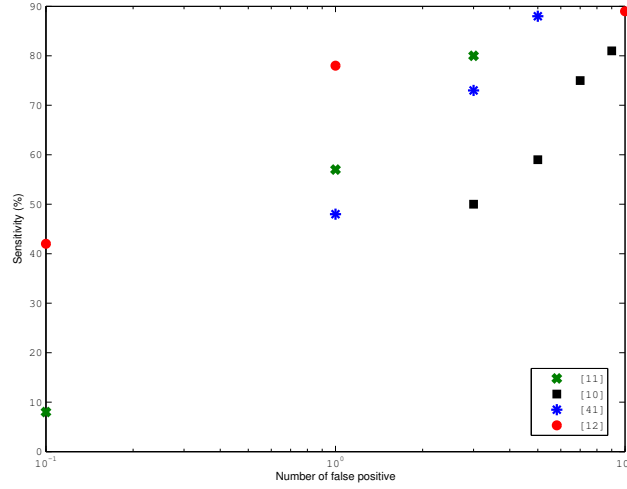


Figure 14: Comparison in terms of FROC of the methods using data from 3.0 Tesla MRI scanner.

type of MRI scanner used (cf., 1.5 *versus* 3.0 Tesla). For each field, the *best performances* obtained in each study were reported in these figures.

The results given in terms of AUC-ROC are depicted in Fig. 12. The results vary between 71% and 97% for some experiments with a 1.5 Tesla MRI scanner and 77% and 95% with a 3.0 Tesla MRI scanner.

The results in regard of sensitivity and specificity are reported in Fig. 13. In the case that the data were collected with a 1.5 Tesla MRI scanner, the sensitivity ranges from 74% to 100% and the specificity from 43% to 93%. For the experiments carried out with a 3.0 Tesla MRI scanner, the sensitivity varies from 60% to 90% and the specificity from 66% to 99%.

Four studies also use FROC analysis to report their results and are reported in Fig. 14.

## 5.2. Comparison

We would like to stress the following findings drawn during the review of the different studies:

1. Quantitatively, it is difficult to make a fair comparison between the different studies reviewed. Different factors come into play to elucidate this fact. Mainly a lack of standardization can be pointed out in regard to experimental evaluation: (i) different datasets are used during the evaluation of the frameworks developed disabling a comparison inter-studies. The same conclusion has been recently drawn by [105] supporting this argument; (ii) the experimental results are not reported with a common metric which leads to the inability to compare the different studies.
2. However, multiple studies reported some performance improvements using multi-parametric imaging techniques instead of mono-parametric imaging techniques. Considering only the most recent studies

proposing CADe-CADx frameworks, the following results can be highlighted. [206] obtained an AUC of 77% using an ensemble learning approach combining the features from the three modalities T<sub>2</sub>-W-DCE-DW MRI, while the results obtained as standalone modality were ranging from 62% to 65%. [187] drawn similar conclusions by using T<sub>2</sub>-W and MRSI modalities as both in standalone and multi-parametric framework with an improved AUC from 57%-76% to 85%. The most recent work of [105] obtained an improved AUC metric from 71%-76% considering each modality separately (e.g., T<sub>2</sub>-W-DCE-DW MRI) to 89% in their multi-parametric framework.

3. The studies comparing particular combination of more than one modality give rise to the same fact ([105, 109, 110, 144]): using three modalities lead to better performances than using any combination of two modalities.
4. Unlike the previous remark 2, no straightforward conclusions can be given regarding the performances of each modality in a standalone framework. The modality being processed by different methods, it does not allow us to conclude if a modality by itself is more suited than another. However, we were able to distinguish some interesting trends which deserves the attention of the community. [187, 192, 193] observed that MRSI is a more suitable modality than T<sub>2</sub>-W to highlight cancers. Moreover, ADC maps have shown a better discriminative power than T<sub>2</sub>-W as well ([94, 150, 206]). Lately, [105] observed that DW modality was more suitable than both DCE and T<sub>2</sub>-W to distinguish CaP in their CADx system.
5. Furthermore, multi-parametric has attracted the attention of both radiologists and computer vision researchers. Indeed, pioneer research groups included new modalities over years when at the same time, new research groups directly introduced multi-parametric CAD systems. These facts lead us to think that CaP researches will benefit from multi-parametric imaging techniques.
6. When focusing on the different modalities used, it can be pointed out that no research reported the use of all modalities in a single framework: MRSI is usually used as a standalone modality and never combined with the three remaining. Nevertheless, this modality has shown some overall good performances at the price of a lower resolution as well as an acquisition time. Moreover, MRSI analysis is more complex in comparison with the other modalities. To our mind, MRSI could contribute in a multi-parametric framework and should be fused with the other modalities.
7. Lately, three studies ([105, 108, 210]) focused on developing a region-based classification in which PZ and CG will be analysed separately instead of jointly. The results provided seem to be promising and which indicates that this strategy should be further investigated.

8. Recent studies are using quantitative features rather than only SI as input to “image classification”. Even if the studies do not allow us to perform a direct comparison, it seems that these quantitative features provide decorrelate information in regard with SI features and should lead to better performances when combined all together.
9. Regarding the methods used in the “image regularisation” (cf., pre-processing, segmentation and registration), it is particularly difficult to distinguish the benefit of a method over another since none of the studies focus on making comparison of these processing stages. The focus is usually entirely based on the “image classification” framework where different methods are directly compared. Note that the performances of a classifier are highly linked with the features vector in input (cf., discriminative power of the features, correlation of the features, etc.), it is not appropriate to affirm that a machine learning method is outperforming another. However, we could identify a trend in which SVM as well as ensemble learning classifiers (e.g., AdaBoost, GentleBoost and random forest) seem to perform better than neural network, LDA or Naive Bayes.
10. We would like to draw the attention of the reader on the feature extraction/selection stage. This processing could reduce the complexity and also find a better feature space for classification. However, few studies are performing such approaches. [133, 134] are successfully applying a scheme to reduce the number of dimensions by selecting the most discriminative features. It allows them to obtain improved performances compared with a classification performed with their initial feature vector. Another group of studies also applied different feature extraction methods ([187–191, 193, 207, 209, 210]). In these specific cases, no comparison is performed against non-dimension reduction case but it is likely that the results obtained are improved.

### 5.3. General discussion

This review leads to some general discussions which could direct to future avenues for research. As previously mentioned, no open multi-parametric dataset is currently available. This fact leads to an impossibility to fairly compare the different algorithms designed over years. Also, the availability of a full multi-parametric MRI dataset, could lead to the development of algorithms which use all the different modalities currently available. Recalling Tab. 2, it can be noted that none of the current works provides a solution using at the same time the four different modalities. Also, all the algorithms are focused on one type of scanner only, either 1.5 Tesla and 3.0 Tesla. A dataset including both these types of imaging could allow development of more generic algorithms.

Analysing the different stages of the CAD work-flow, it is seen that the actual CAD systems do not include all the different pre-processing steps. It could be interesting to evaluate the improvement using these pre-processing steps on the final results obtained after the classification. Regarding segmentation and

registration of the prostate, CAD systems could greatly benefit from specific research in these areas which could lead to a better automation of those systems. Moreover, other methods specific to segmentation and registration which are not actually used in CAD systems could also perform better than the ones currently used in CADs.

Regarding the classification framework, it seems that the current well-known pattern recognition methods have been widely studied. However, more investigations should be carried out regarding the feature detection stage. Lately, histogram-based features have shown good capabilities in the field of computer vision and could be further investigated. Only one study by [110] used some of these features.

An important point allowing a fair comparison between methods resides in the fact that no universal evaluation model and metric has been defined by the research community allowing such comparison. Usually, it is quite common to choose an evaluation model which fits the dataset limitations, usually the size. Regarding the evaluation, the community should agree on a standard metric to measure the performance of the algorithms designed.

Finally, we would like to focus the attentions of the reader on the availability of a multi-parametric dataset MRI provided by the authors of this review, from a 1.5 Tesla General Electric scanner and a 3.0 Tesla Siemens scanner. This dataset will be available at the following website address: <http://visor.udg.edu/dataset>. The dataset is composed of the four modalities discussed in this review with their corresponding ground-truth images. For each scanner type, each subset will be composed of twenty patients with cancerous lesions and ten healthy patients. In addition of the repository activity, this website will aim at providing comparison between algorithms developed by the research community.

## **6. Conclusion**

This review presented an overview and gave a staging of the research related to CAD development for CaP using multi-parametric MRI data. We aimed at providing background information regarding multi-parametric MRI imaging techniques. A work-flow describing the CAD stages were proposed. The methods used in the literature for each of this stage were reviewed. The results of the available CAD systems were briefly reviewed. Subsequently, an insight discussion were given to conclude this survey. Additionally, a multi-parametric dataset will be made available to the research community in order to provide some solutions to outcomes pointed out during the review.

## **7. Acknowledgement**

G. Lemaître was supported by the Generalitat de Catalunya (grant nb. FI-DGR2012) and partly by the Mediterranean Office for Youth (grant nb. 2011/018/06).



We would like to acknowledge Sharad Nagappa for all the discussions involved and his precious advices and corrections regarding the redaction of this entire manuscript.

We would like also to thank the Clinica Girona (Catalunya, Espanya) and the Centre Hospitalier of Dijon (France) for providing the MRI images used in this review.

## References

- [1] Agalliu, I., Gern, R., Leanza, S., Burk, R.D., 2009. Associations of high-grade prostate cancer with BRCA1 and BRCA2 founder mutations. *Clin. Cancer Res.* 15, 1112–1120.
- [2] Ahmed, N., Natarajan, T., Rao, K., 1974. Discrete cosine transform. *Computers, IEEE Transactions on C-23*, 90–93.
- [3] Akin, O., Sala, E., Moskowitz, C.S., Kuroiwa, K., Ishill, N.M., Pucar, D., Scardino, P.T., Hricak, H., 2006. Transition zone prostate cancers: features, detection, localization, and staging at endorectal MR imaging. *Radiology* 239, 784–792.
- [4] Alexander, D.D., Mink, P.J., Cushing, C.A., Scurman, B., 2010. A review and meta-analysis of prospective studies of red and processed meat intake and prostate cancer. *Nutr J* 9, 50.
- [5] American Cancer Society, A.C., 2010. Cancer Facts and Figures 2010. <http://www.cancer.org/research/cancerfactsfigures>. URL: <http://www.cancer.org/research/cancerfactsfigures>. accessed: 2013-08-01.
- [6] American Cancer Society, A.C., 2013. Cancer Facts and Figures 2013. <http://www.cancer.org/research/cancerfactsfigures>. Accessed: 2013-08-01.
- [7] Ampeliotis, D., Anonakoudi, A., Berberidis, K., Psarakis, E.Z., 2007. Computer aided detection of prostate cancer using fused information from dynamic contrast enhanced and morphological magnetic resonance images, in: *IEEE International Conference on Signal Processing and Communications*, pp. 888–891.
- [8] Ampeliotis, D., Anonakoudi, A., Berberidis, K., Psarakis, E.Z., Kounoudes, A., 2008. A computer-aided system for the detection of prostate cancer based on magnetic resonance image analysis, in: *International Symposium on Communications, Control and Signal Processing*.
- [9] Amundadottir, L.T., Sulem, P., Gudmundsson, J., Helgason, A., Baker, A., Agnarsson, B.A., Sigurdsson, A., Benediktsdottir, K.R., Cazier, J.B., Sainz, J., Jakobsdottir, M., Kostic, J., Magnúsdottir, D.N., Ghosh, S., Agnarsson, K., Birgisdottir, B., Le Roux, L., Olafsdottir, A., Blondal, T., Andresdottir, M., Gretarsdottir, O.S., Bergthorsson, J.T., Gudbjartsson, D., Gylfason, A., Thorleifsson, G., Manolescu, A., Kristjansson, K., Geirsson, G., Isaksson, H., Douglas, J., Johansson, J.E., Balter, K., Wiklund, F., Montie, J.E., Yu, X., Suarez, B.K., Ober, C., Cooney, K.A., Gronberg, H., Catalona, W.J., Einarsson, G.V., Barkardottir, R.B., Gulcher, J.R., Kong, A., Thorsteinsdottir, U., Stefansson, K., 2006. A common variant associated with prostate cancer in European and African populations. *Nat. Genet.* 38, 652–658.
- [10] Andriole, G.L., Crawford, E.D., Grubb, R.L., Buys, S.S., Chia, D., Church, T.R., Fouad, M.N., Gelmann, E.P., Kvale, P.A., Reding, D.J., Weissfeld, J.L., Yokochi, L.A., O'Brien, B., Clapp, J.D., Rathmell, J.M., Riley, T.L., Hayes, R.B., Kramer, B.S., Izmirlian, G., Miller, A.B., Pinsky, P.F., Prorok, P.C., Gohagan, J.K., Berg, C.D., 2009. Mortality results from a randomized Prostate-cancer screening trial. *New England Journal of Medicine* 360, 1310–1319.
- [11] Antic, T., Peng, Y., Jiang, Y., Giger, M.L., Eggen, S., Oto, A., 2013. A study of T2-weighted MR image texture features and diffusion-weighted MR image features for computer-aided diagnosis of prostate cancer, in: *Proc. SPIE 8670, Medical Imaging 2013: Computer-Aided Diagnosis*, pp. 86701H–86701H–6.
- [12] Artan, Y., Haider, M.A., Langer, D.L., van der Kwast, T.H., Evans, A.J., Yang, Y., Wernick, M.N., Trachtenberg, J., Yetik, I.S., 2010. Prostate cancer localization with multispectral MRI using cost-sensitive support vector machines and conditional random fields. *IEEE Trans Image Process* 19, 2444–2455.
- [13] Artan, Y., Langer, D., Haider, M., Van der Kwast, T.H., Evans, A., Wernick, M., Yetik, I., 2009. Prostate cancer

- segmentation with multispectral MRI using cost-sensitive Conditional Random Fields, in: Biomedical Imaging: From Nano to Macro, 2009. ISBI '09. IEEE International Symposium on, pp. 278–281.
- [14] Awwad, H.M., Geisel, J., Obeid, R., 2012. The role of choline in prostate cancer. *Clin. Biochem.* 45, 1548–1553.
  - [15] Barentsz, J.O., Richenberg, J., Clements, R., Choyke, P., Verma, S., Villeirs, G., Rouviere, O., Logager, V., Futterer, J.J., 2012. ESUR prostate MR guidelines 2012. *Eur Radiol* 22, 746–757.
  - [16] Belkin, M., Niyogi, P., 2001. Laplacian eigenmaps and spectral techniques for embedding and clustering, in: *Advances in Neural Information Processing Systems 14*, MIT Press. pp. 585–591.
  - [17] Belongie, S., Malik, J., Puzicha, J., 2002. Shape matching and object recognition using shape contexts. *Pattern Analysis and Machine Intelligence, IEEE Transactions on* 24, 509–522.
  - [18] Benassi, A., Cohen, S., Ista, J., 1998. Identifying the multifractional function of a Gaussian process. *Statistics & Probability Letters* 39, 337 – 345.
  - [19] Bishop, C.M., 2006. *Pattern recognition and machine learning*. Springer-Verlag New York, Inc., Secaucus, NJ, USA.
  - [20] Boser, B.E., Guyon, I.M., Vapnik, V.N., 1992. A training algorithm for optimal margin classifiers, in: *Proceedings of the Fifth Annual Workshop on Computational Learning Theory*, ACM, New York, NY, USA. pp. 144–152.
  - [21] Bourdumis, A., Papatsoris, A.G., Chrisofos, M., Efstathiou, E., Skolarikos, A., Deliveliotis, C., 2010. The novel prostate cancer antigen 3 (PCA3) biomarker. *Int Braz J Urol* 36, 665–668.
  - [22] Breiman, L., 2001. Random forests. *Machine Learning* 45, 5–32.
  - [23] Brenner, J., Chinnaiyan, A., Tomlins, S., 2013. ETS fusion genes in prostate cancer, in: Tindall, D.J. (Ed.), *Prostate Cancer*. Springer New York. volume 16 of *Protein Reviews*, pp. 139–183.
  - [24] Buades, A., Coll, B., Morel, J., 2005. A review of image denoising algorithms, with a new one. *Simul* 4, 490–530.
  - [25] Byrd, R.H., Lu, P., Nocedal, J., Zhu, C., 1995. A limited memory algorithm for bound constrained optimization. *SIAM J. Sci. Comput.* 16, 1190–1208.
  - [26] Carrol, C.L., Sommer, F.G., McNeal, J.E., Stamey, T.A., 1987. The abnormal prostate: MR imaging at 1.5 T with histopathologic correlation. *Radiology* 163, 521–525.
  - [27] Castorina, P., Delsanto, P.P., Guiot, C., 2006. Classification scheme for phenomenological universalities in growth problems in physics and other sciences. *Phys. Rev. Lett.* 96, 188701.
  - [28] Chan, H.P., Sahiner, B., Helvie, M.A., Petrick, N., Roubidoux, M.A., Wilson, T.E., Adler, D.D., Paramagul, C., Newman, J.S., Sanjay-Gopal, S., 1999. Improvement of radiologists' characterization of mammographic masses by using computer-aided diagnosis: an ROC study. *Radiology* 212, 817–827.
  - [29] Chan, I., Wells, W., Mulkern, R.V., Haker, S., Zhang, J., Zou, K.H., Maier, S.E., Tempany, C.M., 2003. Detection of prostate cancer by integration of line-scan diffusion, T2-mapping and T2-weighted magnetic resonance imaging; a multichannel statistical classifier. *Med Phys* 30, 2390–2398.
  - [30] Chappelow, J., Bloch, B.N., Rofsky, N., Genega, E., Lenkinski, R., DeWolf, W., Madabhushi, A., 2011. Elastic registration of multimodal prostate MRI and histology via multiattribute combined mutual information. *Med Phys* 38, 2005–2018.
  - [31] Chen, L., Weng, Z., Goh, L., Garland, M., 2002. An efficient algorithm for automatic phase correction of {NMR} spectra based on entropy minimization. *Journal of Magnetic Resonance* 158, 164 – 168.
  - [32] Chilali, O., Ouzzane, A., Diaf, M., Betrouni, N., 2014. A survey of prostate modeling for image analysis. *Computers in Biology and Medicine* 53, 190 – 202.
  - [33] Choi, Y.J., Kim, J.K., Kim, N., Kim, K.W., Choi, E.K., Cho, K.S., 2007. Functional MR imaging of prostate cancer. *Radiographics* 27, 63–75.
  - [34] Chou, R., Crosswell, J.M., Dana, T., Bougatsos, C., Blazina, I., Fu, R., Gleitsmann, K., Koenig, H.C., Lam, C., Maltz, A., Ruge, J.B., Lin, K., 2011. Screening for prostate cancer: a review of the evidence for the U.S. Preventive Services Task Force. *Ann. Intern. Med.* 155, 762–771.

- [35] Cohen, R.J., Shannon, B.A., Phillips, M., Moorin, R.E., Wheeler, T.M., Garrett, K.L., 2008. Central zone carcinoma of the prostate gland: a distinct tumor type with poor prognostic features. *J. Urol.* 179, 1762–1767.
- [36] Coifman, R., Wickerhauser, M., 1992. Entropy-based algorithms for best basis selection. *Information Theory, IEEE Transactions on* 38, 713–718.
- [37] Coleman, T., Li, Y., 1993. An interior trust region approach for nonlinear minimization subject to bounds. Technical Report. Cornell University.
- [38] Cootes, T.F., Taylor, C.J., Cooper, D.H., Graham, J., 1995. Active shape models—Their training and application. *Comput. Vis. Image Underst.* 61, 38–59.
- [39] Costello, L.C., Franklin, R.B., 2006. The clinical relevance of the metabolism of prostate cancer; zinc and tumor suppression: connecting the dots. *Mol. Cancer* 5, 17.
- [40] Cruz, M., Tsuda, K., Narumi, Y., Kuroiwa, Y., Nose, T., Kojima, Y., Okuyama, A., Takahashi, S., Aozasa, K., Barentsz, J.O., Nakamura, H., 2002. Characterization of low-intensity lesions in the peripheral zone of prostate on pre-biopsy endorectal coil MR imaging. *Eur Radiol* 12, 357–365.
- [41] Dalal, N., Triggs, B., 2005. Histograms of oriented gradients for human detection, in: *Computer Vision and Pattern Recognition, 2005. CVPR 2005. IEEE Computer Society Conference on*, pp. 886–893 vol. 1.
- [42] Daugman, J.G., 1985. Uncertainty relation for resolution in space, spatial frequency, and orientation optimized by two-dimensional visual cortical filters. *J Opt Soc Am A* 2, 1160–1169.
- [43] Dean, J.C., Ilvento, C.C., 2006. Improved cancer detection using computer-aided detection with diagnostic and screening mammography: prospective study of 104 cancers. *AJR Am J Roentgenol* 187, 20–28.
- [44] Delongchamps, N.B., Peyromaure, M., Schull, A., Beuvon, F., Bouazza, N., Flam, T., Zerbib, M., Muradyan, N., Legman, P., Cornud, F., 2013. Prebiopsy magnetic resonance imaging and prostate cancer detection: comparison of random and targeted biopsies. *J. Urol.* 189, 493–499.
- [45] Delpierre, C., Lamy, S., Kelly-Irving, M., Molinie, F., Velten, M., Tretarre, B., Woronoff, A.S., Buemi, A., Lapotre-Ledoux, B., Bara, S., Guizard, A.V., Colonna, M., Grosclaude, P., 2013. Life expectancy estimates as a key factor in over-treatment: the case of prostate cancer. *Cancer Epidemiol* 37, 462–468.
- [46] Devos, A., Lukas, L., Suykens, J.A., Vanhamme, L., Tate, A.R., Howe, F.A., Majos, C., Moreno-Torres, A., van der Graaf, M., Arus, C., Van Huffel, S., 2004. Classification of brain tumours using short echo time 1H MR spectra. *J. Magn. Reson.* 170, 164–175.
- [47] Doo, K.W., Sung, D.J., Park, B.J., Kim, M.J., Cho, S.B., Oh, Y.W., Ko, Y.H., Yang, K.S., 2012. Detectability of low and intermediate or high risk prostate cancer with combined T2-weighted and diffusion-weighted MRI. *Eur Radiol* 22, 1812–1819.
- [48] Efron, B., 1983. Estimating the error rate of a prediction rule: Improvement on cross-validation. *Journal of the American Statistical Association* 78, pp. 316–331.
- [49] Etzioni, R., Penson, D.F., Legler, J.M., di Tommaso, D., Boer, R., Gann, P.H., Feuer, E.J., 2002. Overdiagnosis due to prostate-specific antigen screening: lessons from U.S. prostate cancer incidence trends. *J. Natl. Cancer Inst.* 94, 981–990.
- [50] Ferlay, J., Shin, H.R., Bray, F., Forman, D., Mathers, C., Parkin, D.M., 2010. Estimates of worldwide burden of cancer in 2008: GLOBOCAN 2008. *Int. J. Cancer* 127, 2893–2917.
- [51] Fodor, I., 2002. A survey of dimension reduction techniques.
- [52] Fred, A., Jain, A., 2005. Combining multiple clusterings using evidence accumulation. *Pattern Analysis and Machine Intelligence, IEEE Transactions on* 27, 835–850.
- [53] Freedman, M.L., Haiman, C.A., Patterson, N., McDonald, G.J., Tandon, A., Waliszewska, A., Penney, K., Steen, R.G., Ardlie, K., John, E.M., Oakley-Girvan, I., Whittemore, A.S., Cooney, K.A., Ingles, S.A., Altshuler, D., Henderson, B.E., Reich, D., 2006. Admixture mapping identifies 8q24 as a prostate cancer risk locus in African-American men. *Proc. Natl.*

Acad. Sci. U.S.A. 103, 14068–14073.

- [54] Freund, Y., Schapire, R., 1997. A decision-theoretic generalization of on-line learning and an application to boosting. *Journal of Computer and System Sciences* 55, 119 – 139.
- [55] Friedman, J., 1989. Regularized discriminant analysis. *Journal of the American Statistical Association* 84, pp. 165–175.
- [56] Friedman, J., Hastie, T., Tibshirani, R., 1998. Additive logistic regression: a statistical view of boosting. *Annals of Statistics* 28, 2000.
- [57] Gabor, D., 1946. Theory of communication. Part 1: The analysis of information. *Electrical Engineers - Part III: Radio and Communication Engineering, Journal of the Institution of* 93, 429–441.
- [58] Ghose, S., Oliver, A., Marti, R., Llado, X., Vilanova, J.C., Freixenet, J., Mitra, J., Sidibe, D., Meriaudeau, F., 2012. A survey of prostate segmentation methodologies in ultrasound, magnetic resonance and computed tomography images. *Comput Methods Programs Biomed* 108, 262–287.
- [59] Giannini, V., Vignati, A., Mazzetti, S., De Luca, M., Bracco, C., Stasi, M., Russo, F., Armando, E., Regge, D., 2013. A prostate CAD system based on multiparametric analysis of DCE T1-w, and DW automatically registered images, in: *Proc. SPIE 8670, Medical Imaging 2013: Computer-Aided Diagnosis*, pp. 86703E–86703E–6.
- [60] Gibbs, P., Tozer, D.J., Liney, G.P., Turnbull, L.W., 2001. Comparison of quantitative T2 mapping and diffusion-weighted imaging in the normal and pathologic prostate. *Magn Reson Med* 46, 1054–1058.
- [61] Giger, M.L., Chan, H.P., Boone, J., 2008. Anniversary paper: History and status of CAD and quantitative image analysis: the role of Medical Physics and AAPM. *Med Phys* 35, 5799–5820.
- [62] Giovannucci, E., Liu, Y., Platz, E.A., Stampfer, M.J., Willett, W.C., 2007. Risk factors for prostate cancer incidence and progression in the health professionals follow-up study. *Int. J. Cancer* 121, 1571–1578.
- [63] Giskeodegard, G.F., Bertilsson, H., Selnaes, K.M., Wright, A.J., Bathen, T.F., Viset, T., Halgunset, J., Angelsen, A., Gribbestad, I.S., Tessem, M.B., 2013. Spermine and citrate as metabolic biomarkers for assessing prostate cancer aggressiveness. *PLoS ONE* 8, e62375.
- [64] Gleason, D.F., 1977. Urologic pathology: The prostate. Lea and Febiger.. chapter The Veteran’s Administration Cooperative Urologic Research Group: histologic grading and clinical staging of prostatic carcinoma. p. 171198.
- [65] van der Graaf, M., Schipper, R.G., Oosterhof, G.O., Schalken, J.A., Verhofstad, A.A., Heerschap, A., 2000. Proton MR spectroscopy of prostatic tissue focused on the detection of spermine, a possible biomarker of malignant behavior in prostate cancer. *MAGMA* 10, 153–159.
- [66] Gribbestad, I., Gjesdal, K., Nilsen, G., Lundgren, S., Hjelstuen, M., Jackson, A., 2005. An introduction to dynamic contrast-enhanced MRI in oncology, in: Jackson, A., Buckley, D., Parker, G. (Eds.), *Dynamic Contrast-Enhanced Magnetic Resonance Imaging in Oncology*. Springer Berlin Heidelberg. Medical Radiology, pp. 1–22.
- [67] Haas, G.P., Delongchamps, N.B., Jones, R.F., Chandan, V., Serio, A.M., Vickers, A.J., Jumbelic, M., Threatte, G., Korets, R., Lilja, H., de la Roza, G., 2007. Needle biopsies on autopsy prostates: sensitivity of cancer detection based on true prevalence. *J. Natl. Cancer Inst.* 99, 1484–1489.
- [68] Hambrock, T., Somford, D.M., Huisman, H.J., van Oort, I.M., Witjes, J.A., Hulsbergen-van de Kaa, C.A., Scheenen, T., Barentsz, J.O., 2011. Relationship between apparent diffusion coefficients at 3.0-T MR imaging and Gleason grade in peripheral zone prostate cancer. *Radiology* 259, 453–461.
- [69] Hambrock, T., Vos, P.C., Hulsbergen-van de Kaa, C.A., Barentsz, J.O., Huisman, H.J., 2013. Prostate cancer: computer-aided diagnosis with multiparametric 3-T MR imaging—effect on observer performance. *Radiology* 266, 521–530.
- [70] Hara, N., Okuizumi, M., Koike, H., Kawaguchi, M., Bilim, V., 2005. Dynamic contrast-enhanced magnetic resonance imaging (DCE-MRI) is a useful modality for the precise detection and staging of early prostate cancer. *Prostate* 62, 140–147.
- [71] Haralick, R., Shanmugam, K., Dinstein, I., 1973. Textural features for image classification. *Systems, Man and Cyber-*

- netics, *IEEE Transactions on SMC-3*, 610–621.
- [72] Hegde, J.V., Mulkern, R.V., Panych, L.P., Fennessy, F.M., Fedorov, A., Maier, S.E., Tempany, C.M., 2013. Multiparametric MRI of prostate cancer: an update on state-of-the-art techniques and their performance in detecting and localizing prostate cancer. *J Magn Reson Imaging* 37, 1035–1054.
  - [73] Heidenreich, A., Abrahamsson, P.A., Artibani, W., Catto, J., Montorsi, F., Van Poppel, H., Wirth, M., Mottet, N., 2013. Early detection of prostate cancer: European Association of Urology recommendation. *Eur. Urol.* 64, 347–354.
  - [74] Hoeks, C.M., Barentsz, J.O., Hambrock, T., Yakar, D., Somford, D.M., Heijmink, S.W., Scheenen, T.W., Vos, P.C., Huisman, H., van Oort, I.M., Witjes, J.A., Heerschap, A., Futterer, J.J., 2011. Prostate cancer: multiparametric MR imaging for detection, localization, and staging. *Radiology* 261, 46–66.
  - [75] Hoffman, R.M., Gilliland, F.D., Eley, J.W., Harlan, L.C., Stephenson, R.A., Stanford, J.L., Albertson, P.C., Hamilton, A.S., Hunt, W.C., Potosky, A.L., 2001. Racial and ethnic differences in advanced-stage prostate cancer: the Prostate Cancer Outcomes Study. *J. Natl. Cancer Inst.* 93, 388–395.
  - [76] Hricak, H., Dooms, G.C., McNeal, J.E., Mark, A.S., Marotti, M., Avallone, A., Pelzer, M., Proctor, E.C., Tanagho, E.A., 1987. MR imaging of the prostate gland: normal anatomy. *AJR Am J Roentgenol* 148, 51–58.
  - [77] Hricak, H., Williams, R.D., Spring, D.B., Moon, K.L., Hedgcock, M.W., Watson, R.A., Crooks, L.E., 1983. Anatomy and pathology of the male pelvis by magnetic resonance imaging. *AJR Am J Roentgenol* 141, 1101–1110.
  - [78] Huch Boni, R.A., Boner, J.A., Lutolf, U.M., Trinkler, F., Pestalozzi, D.M., Krestin, G.P., 1995. Contrast-enhanced endorectal coil MRI in local staging of prostate carcinoma. *J Comput Assist Tomogr* 19, 232–237.
  - [79] Hugosson, J., Carlsson, S., Aus, G., Bergdahl, S., Khatami, A., Lodding, P., Pihl, C.G., Stranne, J., Holmberg, E., Lilja, H., 2010. Mortality results from the Göteborg randomised population-based prostate-cancer screening trial. *Lancet Oncol.* 11, 725–732.
  - [80] Huisman, H., Vos, P., Litjens, G., Hambrock, T., Barentsz, J., 2010. Computer aided detection of prostate cancer using T2, DWI and DCE MRI: methods and clinical applications, in: *Proceedings of the 2010 international conference on Prostate cancer imaging: computer-aided diagnosis, prognosis, and intervention*, Springer-Verlag, Berlin, Heidelberg. pp. 4–14.
  - [81] Huisman, T.A., 2003. Diffusion-weighted imaging: basic concepts and application in cerebral stroke and head trauma. *Eur Radiol* 13, 2283–2297.
  - [82] Itou, Y., Nakanishi, K., Narumi, Y., Nishizawa, Y., Tsukuma, H., 2011. Clinical utility of apparent diffusion coefficient (ADC) values in patients with prostate cancer: can ADC values contribute to assess the aggressiveness of prostate cancer? *J Magn Reson Imaging* 33, 167–172.
  - [83] Jager, G.J., Ruijter, E.T., van de Kaa, C.A., de la Rosette, J.J., Oosterhof, G.O., Thornbury, J.R., Ruijs, S.H., Barentsz, J.O., 1997. Dynamic TurboFLASH subtraction technique for contrast-enhanced MR imaging of the prostate: correlation with histopathologic results. *Radiology* 203, 645–652.
  - [84] Jolliffe, I.T., 2002. *Principal Component Analysis*. Second ed., Springer.
  - [85] Jungke, M., Von Seelen, W., Bielke, G., Meindl, S., Grigat, M., Pfannenstiel, P., 1987. A system for the diagnostic use of tissue characterizing parameters in NMR-tomography, in: *Proc. of Information Processing in Medical Imaging*, pp. 471–481.
  - [86] Kaji, Y., Kurhanewicz, J., Hricak, H., Sokolov, D.L., Huang, L.R., Nelson, S.J., Vigneron, D.B., 1998. Localizing prostate cancer in the presence of postbiopsy changes on MR images: role of proton MR spectroscopic imaging. *Radiology* 206, 785–790.
  - [87] Kelm, B.M., Menze, B.H., Zechmann, C.M., Baudendistel, K.T., Hamprecht, F.A., 2007. Automated estimation of tumor probability in prostate magnetic resonance spectroscopic imaging: pattern recognition vs quantification. *Magn Reson Med* 57, 150–159.

- [88] Kim, J.K., Hong, S.S., Choi, Y.J., Park, S.H., Ahn, H., Kim, C.S., Cho, K.S., 2005. Wash-in rate on the basis of dynamic contrast-enhanced MRI: usefulness for prostate cancer detection and localization. *J Magn Reson Imaging* 22, 639–646.
- [89] Kirkham, A.P., Emberton, M., Allen, C., 2006. How good is MRI at detecting and characterising cancer within the prostate? *Eur. Urol.* 50, 1163–1174.
- [90] Kirsch, R., 1971. Computer determination of the constituent structure of biological images . *Computers and Biomedical Research* 4, 315 – 328.
- [91] Klein, S., van der Heide, U.A., Lips, I.M., van Vulpen, M., Staring, M., Pluim, J.P., 2008. Automatic segmentation of the prostate in 3D MR images by atlas matching using localized mutual information. *Med Phys* 35, 1407–1417.
- [92] Koh, D.M., Collins, D.J., 2007. Diffusion-weighted MRI in the body: applications and challenges in oncology. *AJR Am J Roentgenol* 188, 1622–1635.
- [93] Kurhanewicz, J., Vigneron, D.B., Hricak, H., Narayan, P., Carroll, P., Nelson, S.J., 1996. Three-dimensional H-1 MR spectroscopic imaging of the in situ human prostate with high (0.24-0.7-cm3) spatial resolution. *Radiology* 198, 795–805.
- [94] Langer, D.L., van der Kwast, T.H., Evans, A.J., Trachtenberg, J., Wilson, B.C., Haider, M.A., 2009. Prostate cancer detection with multi-parametric MRI: logistic regression analysis of quantitative T2, diffusion-weighted imaging, and dynamic contrast-enhanced MRI. *J Magn Reson Imaging* 30, 327–334.
- [95] Langerak, T.R., van der Heide, U.A., Kotte, A.N., Viergever, M.A., van Vulpen, M., Pluim, J.P., 2010. Label fusion in atlas-based segmentation using a selective and iterative method for performance level estimation (SIMPLE). *IEEE Trans Med Imaging* 29, 2000–2008.
- [96] Le Bihan, D., Breton, E., Lallemand, D., Aubin, M.L., Vignaud, J., Laval-Jeantet, M., 1988. Separation of diffusion and perfusion in intravoxel incoherent motion MR imaging. *Radiology* 168, 497–505.
- [97] Le Bihan, D., Breton, E., Lallemand, D., Grenier, P., Cabanis, E., Laval-Jeantet, M., 1986. MR imaging of intravoxel incoherent motions: application to diffusion and perfusion in neurologic disorders. *Radiology* 161, 401–407.
- [98] Lemaître, G., 2011. Absolute quantification at 3 T. Master’s thesis. Université de Bourgogne, Heriot-Watt University, Universitat de Girona.
- [99] Leung, T., Malik, J., 2001. Representing and recognizing the visual appearance of materials using three-dimensional textons. *International Journal of Computer Vision* 43, 29–44.
- [100] Li, F., Aoyama, M., Shiraishi, J., Abe, H., Li, Q., Suzuki, K., Engelmann, R., Sone, S., Macmahon, H., Doi, K., 2004. Radiologists’ performance for differentiating benign from malignant lung nodules on high-resolution CT using computer-estimated likelihood of malignancy. *AJR Am J Roentgenol* 183, 1209–1215.
- [101] Lieber, C.A., Mahadevan-Jansen, A., 2003. Automated method for subtraction of fluorescence from biological Raman spectra. *Appl Spectrosc* 57, 1363–1367.
- [102] Liney, G.P., Knowles, A.J., Manton, D.J., Turnbull, L.W., Blackband, S.J., Horsman, A., 1996a. Comparison of conventional single echo and multi-echo sequences with a fast spin-echo sequence for quantitative T2 mapping: application to the prostate. *J Magn Reson Imaging* 6, 603–607.
- [103] Liney, G.P., Lowry, M., Turnbull, L.W., Manton, D.J., Knowles, A.J., Blackband, S.J., Horsman, A., 1996b. Proton MR T2 maps correlate with the citrate concentration in the prostate. *NMR Biomed* 9, 59–64.
- [104] Liney, G.P., Turnbull, L.W., Lowry, M., Turnbull, L.S., Knowles, A.J., Horsman, A., 1997. In vivo quantification of citrate concentration and water T2 relaxation time of the pathologic prostate gland using 1H MRS and MRI. *Magn Reson Imaging* 15, 1177–1186.
- [105] Litjens, G., Debats, O., Barentsz, J., Karssemeijer, N., Huisman, H., 2014a. Computer-aided detection of prostate cancer in MRI. *Medical Imaging, IEEE Transactions on* 33, 1083–1092.
- [106] Litjens, G., Debats, O., van de Ven, W., Karssemeijer, N., Huisman, H., 2012a. A pattern recognition approach to zonal segmentation of the prostate on MRI. *Med Image Comput Comput Assist Interv* 15, 413–420.

- [107] Litjens, G., Toth, R., van de Ven, W., Hoeks, C., Kerkstra, S., van Ginneken, B., Vincent, G., Guillard, G., Birbeck, N., Zhang, J., Strand, R., Malmberg, F., Ou, Y., Davatzikos, C., Kirschner, M., Jung, F., Yuan, J., Qiu, W., Gao, Q., Edwards, P.E., Maan, B., van der Heijden, F., Ghose, S., Mitra, J., Dowling, J., Barratt, D., Huisman, H., Madabhushi, A., 2014b. Evaluation of prostate segmentation algorithms for MRI: the PROMISE12 challenge. *Med Image Anal* 18, 359–373.
- [108] Litjens, G.J.S., Barentsz, J.O., Karssemeijer, N., Huisman, H.J., 2012b. Automated computer-aided detection of prostate cancer in MR images: from a whole-organ to a zone-based approach, in: *Proc. SPIE 8315, Medical Imaging 2012: Computer-Aided Diagnosis*, pp. 83150G–83150G–6.
- [109] Litjens, G.J.S., Vos, P.C., Barentsz, J.O., Karssemeijer, N., Huisman, H.J., 2011. Automatic computer aided detection of abnormalities in multi-parametric prostate MRI, in: *Proc. SPIE 7963, Medical Imaging 2011: Computer-Aided Diagnosis*, pp. 79630T–79630T–7.
- [110] Liu, P., Wang, S., Turkbey, B., Grant, K. and Pinto, P.C.P., Wood, B.J., Summers, R.M., 2013. A prostate cancer computer-aided diagnosis system using multimodal magnetic resonance imaging and targeted biopsy labels, in: *Proc. SPIE 8670, Medical Imaging 2013: Computer-Aided Diagnosis*, pp. 86701G–86701G–6.
- [111] Liu, W., Turkbey, B., Senegas, J., Remmele, S., Xu, S., Kruecker, J., Bernardo, M., Wood, B.J., Pinto, P.A., Choyke, P.L., 2011. Accelerated T2 mapping for characterization of prostate cancer. *Magn Reson Med* 65, 1400–1406.
- [112] Liu, X., Langer, D.L., Haider, M.A., Yang, Y., Wernick, M.N., Yetik, I.S., 2009. Prostate cancer segmentation with simultaneous estimation of Markov random field parameters and class. *IEEE Trans Med Imaging* 28, 906–915.
- [113] Lopes, R., Ayache, A., Makni, N., Puech, P., Villers, A., Mordon, S., Betrouni, N., 2011. Prostate cancer characterization on MR images using fractal features. *Med Phys* 38, 83–95.
- [114] Lu-Yao, G.L., Albertsen, P.C., Moore, D.F., Shih, W., Lin, Y., DiPaola, R.S., Barry, M.J., Zietman, A., O’Leary, M., Walker-Corkery, E., Yao, S.L., 2009. Outcomes of localized prostate cancer following conservative management. *JAMA* 302, 1202–1209.
- [115] Lv, D., Guo, X., Wang, X., Zhang, J., Fang, J., 2009. Computerized characterization of prostate cancer by fractal analysis in MR images. *J Magn Reson Imaging* 30, 161–168.
- [116] Ma, R.W., Chapman, K., 2009. A systematic review of the effect of diet in prostate cancer prevention and treatment. *J Hum Nutr Diet* 22, 187–199.
- [117] Madabhushi, A., Udupa, J., Souza, A., 2006. Generalized scale: Theory, algorithms, and application to image inhomogeneity correction. *Computer Vision and Image Understanding* 101, 100 – 121.
- [118] Madabhushi, A., Udupa, J.K., 2006. New methods of MR image intensity standardization via generalized scale. *Med Phys* 33, 3426–3434.
- [119] Maintz, J.B., Viergever, M.A., 1998. A survey of medical image registration. *Med Image Anal* 2, 1–36.
- [120] Mallat, S., 2008. A wavelet tour of signal processing, Third Edition: The sparse way. 3rd ed., Academic Press.
- [121] Manjon, J.V., Carbonell-Caballero, J., Lull, J.J., Garcia-Marti, G., Marti-Bonmati, L., Robles, M., 2008. MRI denoising using non-local means. *Med Image Anal* 12, 514–523.
- [122] Matulewicz, L., Jansen, J.F., Bokacheva, L., Vargas, H.A., Akin, O., Fine, S.W., Shukla-Dave, A., Eastham, J.A., Hricak, H., Koutcher, J.A., Zakian, K.L., 2013. Anatomic segmentation improves prostate cancer detection with artificial neural networks analysis of 1H magnetic resonance spectroscopic imaging. *Journal of Magnetic Resonance Imaging* , n/a–n/a.
- [123] Mazzetti, S., De Luca, M., Bracco, C., Vignati, A., Giannini, V., Stasi, M., Russo, F., Armando, E., Agliozzo, S., Regge, D., 2011. A CAD system based on multi-parametric analysis for cancer prostate detection on DCE-MRI, in: *Proc. SPIE 7963, Medical Imaging 2011: Computer-Aided Diagnosis*, pp. 79633Q–79633Q–7.
- [124] McNeal, J.E., Redwine, E.A., Freiha, F.S., Stamey, T.A., 1988. Zonal distribution of prostatic adenocarcinoma. Correlation with histologic pattern and direction of spread. *Am. J. Surg. Pathol.* 12, 897–906.

- [125] Metz, C.E., 2006. Receiver operating characteristic analysis: a tool for the quantitative evaluation of observer performance and imaging systems. *J Am Coll Radiol* 3, 413–422.
- [126] Middleton, D., Esposito, R., 1968. Simultaneous optimum detection and estimation of signals in noise. *Information Theory, IEEE Transactions on* 14, 434–444.
- [127] Mitra, J., 2012. Multimodal image registration applied to magnetic resonance and ultrasound prostatic images. Ph.D. thesis. Universitat de Girona and Université de Bourgogne.
- [128] Mitra, J., Kato, Z., Marti, R., Oliver, A., Llado, X., Sidibe, D., Ghose, S., Vilanova, J.C., Comet, J., Meriaudeau, F., 2012. A spline-based non-linear diffeomorphism for multimodal prostate registration. *Med Image Anal* 16, 1259–1279.
- [129] Mitra, J., Marti, R., Oliver, A., Llado, X., Vilanova, J.C., Meriaudeau, F., 2011. A comparison of thin-plate splines with automatic correspondences and B-splines with uniform grids for multimodal prostate registration, in: *Society of Photo-Optical Instrumentation Engineers (SPIE) Conference Series*.
- [130] Mohan, J., Krishnaveni, V., Guo, Y., 2014. A survey on the magnetic resonance image denoising methods. *Biomedical Signal Processing and Control* 9, 56 – 69.
- [131] Moore, C.M., Ridout, A., Emberton, M., 2013. The role of MRI in active surveillance of prostate cancer. *Curr Opin Urol* 23, 261–267.
- [132] Morgan, R., Boxall, A., Bhatt, A., Bailey, M., Hindley, R., Langley, S., Whitaker, H.C., Neal, D.E., Ismail, M., Whitaker, H., Annels, N., Michael, A., Pandha, H., 2011. Engrailed-2 (EN2): a tumor specific urinary biomarker for the early diagnosis of prostate cancer. *Clin. Cancer Res.* 17, 1090–1098.
- [133] Niaf, E., Rouviere, O., Mege-Lechevallier, F., Bratan, F., Lartizien, C., 2012. Computer-aided diagnosis of prostate cancer in the peripheral zone using multiparametric MRI. *Phys Med Biol* 57, 3833–3851.
- [134] Niaf, E., Rouviere, O., Lartizien, C., 2011. Computer-aided diagnosis for prostate cancer detection in the peripheral zone via multisequence MRI, in: *Proc. SPIE 7963, Medical Imaging 2011: Computer-Aided Diagnosis*.
- [135] van Niekerk, C.G., Witjes, J.A., Barentsz, J.O., van der Laak, J.A., Hulsbergen-van de Kaa, C.A., 2013. Microvasculature in transition zone prostate tumors resembles normal prostatic tissue. *Prostate* 73, 467–475.
- [136] Noguchi, M., Stamey, T.A., McNeal, J.E., Yemoto, C.M., 2001. Relationship between systematic biopsies and histological features of 222 radical prostatectomy specimens: lack of prediction of tumor significance for men with nonpalpable prostate cancer. *J. Urol.* 166, 104–109.
- [137] Nowak, R., 1999. Wavelet-based Rician noise removal for magnetic resonance imaging. *Image Processing, IEEE Transactions on* 8, 1408–1419.
- [138] Nyul, L.G., Udupa, J.K., 1999. On standardizing the MR image intensity scale. *Magn Reson Med* 42, 1072–1081.
- [139] Nyul, L.G., Udupa, J.K., Zhang, X., 2000. New variants of a method of MRI scale standardization. *IEEE Trans Med Imaging* 19, 143–150.
- [140] Ojala, T., Pietikäinen, M., Harwood, D., 1996. A comparative study of texture measures with classification based on featured distributions. *Pattern Recognition* 29, 51–59.
- [141] Osorio-Garcia, M., Croitor Sava, A., Sima, D.M., Nielsen, F., Himmelreich, U., Van Huffel, S., 2012. Magnetic Resonance Spectroscopy. InTech. chapter Quantification improvements of 1H MRS Signals. pp. 1–27.
- [142] Oster, G., Lamerato, L., Glass, A.G., Richert-Boe, K.E., Lopez, A., Chung, K., Richhariya, A., Dodge, T., Wolff, G.G., Balakumaran, A., Edelsberg, J., 2013. Natural history of skeletal-related events in patients with breast, lung, or prostate cancer and metastases to bone: a 15-year study in two large US health systems. *Support Care Cancer* 21, 3279–3286.
- [143] Ozer, S., Haider, M., Langer, D.L., Van der Kwast, T.H., Evans, A., Wernick, M., Trachtenberg, J., Yetik, I., 2009. Prostate cancer localization with multispectral MRI based on Relevance Vector Machines, in: *Biomedical Imaging: From Nano to Macro, 2009. ISBI '09. IEEE International Symposium on*, pp. 73–76.
- [144] Ozer, S., Langer, D.L., Liu, X., Haider, M.A., van der Kwast, T.H., Evans, A.J., Yang, Y., Wernick, M.N., Yetik, I.S.,



2010. Supervised and unsupervised methods for prostate cancer segmentation with multispectral MRI. *Med Phys* 37, 1873–1883.
- [145] Padhani, A.R., 2002. Dynamic contrast-enhanced MRI in clinical oncology: current status and future directions. *J Magn Reson Imaging* 16, 407–422.
- [146] Padhani, A.R., 2011. Integrating multiparametric prostate MRI into clinical practice. *Cancer Imaging* 11 Spec No A, 27–37.
- [147] Parfait, S., 2010. Classification de spectres et recherche de biomarqueurs en spectroscopie par résonance magnétique nucléaire du proton dans les tumeurs prostatiques. Ph.D. thesis. Université de Bourgogne.
- [148] Parfait, S., Walker, P., Crhange, G., Tizon, X., Mitran, J., 2012. Classification of prostate magnetic resonance spectra using Support Vector Machine. *Biomedical Signal Processing and Control* 7, 499 – 508.
- [149] Peng, H., Long, F., Ding, C., 2005. Feature selection based on mutual information criteria of max-dependency, max-relevance, and min-redundancy. *Pattern Analysis and Machine Intelligence, IEEE Transactions on* 27, 1226–1238.
- [150] Peng, Y., Jiang, Y., Yang, C., Brown, J., Antic, T., Sethi, I., Schmid-Tannwald, C., Giger, M., Eggener, S., Oto, A., 2013. Quantitative analysis of multiparametric prostate MR images: differentiation between prostate cancer and normal tissue and correlation with Gleason score—a computer-aided diagnosis development study. *Radiology* 267, 787–796.
- [151] Petrick, N., Haider, M., Summers, R.M., Yeshwant, S.C., Brown, L., Iuliano, E.M., Louie, A., Choi, J.R., Pickhardt, P.J., 2008. CT colonography with computer-aided detection as a second reader: observer performance study. *Radiology* 246, 148–156.
- [152] Pijnappel, W., van den Boogaart, A., de Beer, R., van Ormondt, D., 1992. SVD-based quantification of magnetic resonance signals. *Journal of Magnetic Resonance* (1969) 97, 122 – 134.
- [153] Pizurica, A., 2002. Image denoising using wavelets and spatial context modeling. Ph.D. thesis. Universiteit Gent.
- [154] Pizurica, A., Philips, W., Lemahieu, I., Acheroy, M., 2003. A versatile wavelet domain noise filtration technique for medical imaging. *IEEE Trans Med Imaging* 22, 323–331.
- [155] Pluim, J., Maintz, J., Viergever, M., 2003. Mutual-information-based registration of medical images: a survey. *IEEE Transactions on Medical Imaging* 22, 986–1004.
- [156] Prewitt, J., 1970. Picture processing and psychohistories. Academic Press. chapter Object enhancement and extraction.
- [157] Provencher, S.W., 1993. Estimation of metabolite concentrations from localized in vivo proton NMR spectra. *Magn Reson Med* 30, 672–679.
- [158] Puech, P., Betrouni, N., Makni, N., Dewalle, A.S., Villers, A., Lemaitre, L., 2009. Computer-assisted diagnosis of prostate cancer using DCE-MRI data: design, implementation and preliminary results. *Int J Comput Assist Radiol Surg* 4, 1–10.
- [159] Quinonero-Candela, J., Girard, A., Rasmussen, C., 2002. Prediction at an Uncertain Input for Gaussian processes and relevance vector machines application to Multiple-Step ahead time-series forecasting. Technical Report. DTU Informatics.
- [160] Quint, L.E., Van Erp, J.S., Bland, P.H., Mandell, S.H., Del Buono, E.A., Grossman, H.B., Glazer, G.M., Gikas, P.W., 1991. Carcinoma of the prostate: MR images obtained with body coils do not accurately reflect tumor volume. *AJR Am J Roentgenol* 156, 511–516.
- [161] Rasmussen, C., Williams, C., 2005. Gaussian processes for machine learning. The MIT Press.
- [162] Ratiney, H., Sdika, M., Coenradie, Y., Cavassila, S., van Ormondt, D., Graveron-Demilly, D., 2005. Time-domain semi-parametric estimation based on a metabolite basis set. *NMR Biomed* 18, 1–13.
- [163] Rish, I., 2001. An empirical study of the naive Bayes classifier, in: *IJCAI 2001 workshop on empirical methods in artificial intelligence*, pp. 41–46.
- [164] Rodriguez, C., Freedland, S.J., Deka, A., Jacobs, E.J., McCullough, M.L., Patel, A.V., Thun, M.J., Calle, E.E., 2007. Body mass index, weight change, and risk of prostate cancer in the Cancer Prevention Study II Nutrition Cohort. *Cancer Epidemiol. Biomarkers Prev.* 16, 63–69.

- [165] Rosenkrantz, A.B., Sabach, A., Babb, J.S., Matza, B.W., Taneja, S.S., Deng, F.M., 2013. Prostate cancer: comparison of dynamic contrast-enhanced MRI techniques for localization of peripheral zone tumor. *AJR Am J Roentgenol* 201, W471–478.
- [166] Roweis, S.T., Saul, L.K., 2000. Nonlinear dimensionality reduction by locally linear embedding. *Science* 290, 2323–2326.
- [167] Rueckert, D., Sonoda, L.I., Hayes, C., Hill, D.L., Leach, M.O., Hawkes, D.J., 1999. Nonrigid registration using free-form deformations: application to breast MR images. *IEEE Trans Med Imaging* 18, 712–721.
- [168] Saeys, Y., Inza, I., Larranaga, P., 2007. A review of feature selection techniques in bioinformatics. *Bioinformatics* 23, 2507–2517.
- [169] Scheidler, J., Hricak, H., Vigneron, D.B., Yu, K.K., Sokolov, D.L., Huang, L.R., Zaloudek, C.J., Nelson, S.J., Carroll, P.R., Kurhanewicz, J., 1999a. Prostate cancer: localization with three-dimensional proton MR spectroscopic imaging—clinicopathologic study. *Radiology* 213, 473–480.
- [170] Scheidler, J., Petsch, R., Muller-Lisse, U., Heuck, A., Reiser, M., 1999b. Echo-planar diffusion-weighted MR imaging of the prostate, in: *Proceedings of the 7th Annual Meeting of ISMRM Philadelphia*, p. 1103.
- [171] Schlemmer, H.P., Merkle, J., Grobholz, R., Jaeger, T., Michel, M.S., Werner, A., Rabe, J., van Kaick, G., 2004. Can pre-operative contrast-enhanced dynamic MR imaging for prostate cancer predict microvessel density in prostatectomy specimens? *Eur Radiol* 14, 309–317.
- [172] Schroder, F.H., Carter, H.B., Wolters, T., van den Bergh, R.C., Gosselaar, C., Bangma, C.H., Roobol, M.J., 2008. Early detection of prostate cancer in 2007. Part 1: PSA and PSA kinetics. *Eur. Urol.* 53, 468–477.
- [173] Schröder, F.H., Hugosson, J., Roobol, M.J., Tammela, T.L., Ciatto, S., Nelen, V., Kwiatkowski, M., Lujan, M., Lilja, H., Zappa, M., Denis, L.J., Recker, F., Pez, A., Määttänen, L., Bangma, C.H., Aus, G., Carlsson, S., Villers, A., Rebillard, X., van der Kwast, T., Kujala, P.M., Blijenberg, B.G., Stenman, U.H., Huber, A., Taari, K., Hakama, M., Moss, S.M., de Koning, H.J., Auvinen, A., 2012. Prostate-cancer mortality at 11 years of follow-up. *New England Journal of Medicine* 366, 981–990.
- [174] Shi, J., Malik, J., 2000. Normalized cuts and image segmentation. *Pattern Analysis and Machine Intelligence, IEEE Transactions on* 22, 888–905.
- [175] Shimofusa, R., Fujimoto, H., Akamata, H., Motoori, K., Yamamoto, S., Ueda, T., Ito, H., 2005. Diffusion-weighted imaging of prostate cancer. *J Comput Assist Tomogr* 29, 149–153.
- [176] Siegel, R., Naishadham, D., Jemal, A., 2013. Cancer statistics, 2013. *CA Cancer J Clin* 63, 11–30.
- [177] Sobel, I., 1970. Camera models and machine perception. Technical Report. DTIC Document.
- [178] Specht, D.F., 1988. Probabilistic neural networks for classification, mapping, or associative memory, in: *Neural Networks, 1988., IEEE International Conference on*, pp. 525–532 vol.1.
- [179] Stamey, T.A., Donaldson, A.N., Yemoto, C.E., McNeal, J.E., Sozen, S., Gill, H., 1998. Histological and clinical findings in 896 consecutive prostates treated only with radical retropubic prostatectomy: epidemiologic significance of annual changes. *J. Urol.* 160, 2412–2417.
- [180] Steinberg, G.D., Carter, B.S., Beaty, T.H., Childs, B., Walsh, P.C., 1990. Family history and the risk of prostate cancer. *Prostate* 17, 337–347.
- [181] Strum, S., Pogliano, D., 2005. What every doctor who treats male patients should know. *PCRI Insights* vol. 8, no. 2.
- [182] Styner, M., Brechbuhler, C., Szckely, G., Gerig, G., 2000. Parametric estimate of intensity inhomogeneities applied to MRI. *Medical Imaging, IEEE Transactions on* 19, 153–165.
- [183] Sung, Y.S., Kwon, H.J., Park, B.W., Cho, G., Lee, C.K., Cho, K.S., Kim, J.K., 2011. Prostate cancer detection on dynamic contrast-enhanced MRI: computer-aided diagnosis versus single perfusion parameter maps. *AJR Am J Roentgenol* 197, 1122–1129.
- [184] Swanson, M.G., Vigneron, D.B., Tran, T.K., Sailasuta, N., Hurd, R.E., Kurhanewicz, J., 2001. Single-voxel oversampled

- J-resolved spectroscopy of in vivo human prostate tissue. *Magn Reson Med* 45, 973–980.
- [185] Taira, A.V., Merrick, G.S., Galbreath, R.W., Andreini, H., Taubenslag, W., Curtis, R., Butler, W.M., Adamovich, E., Wallner, K.E., 2010. Performance of transperineal template-guided mapping biopsy in detecting prostate cancer in the initial and repeat biopsy setting. *Prostate Cancer Prostatic Dis.* 13, 71–77.
  - [186] Tipping, M., 2001. Sparse Bayesian learning and the relevance vector machine. *Journal of Machine Learning Research* 1, 211–244.
  - [187] Tiwari, P., Kurhanewicz, J., Madabhushi, A., 2013. Multi-kernel graph embedding for detection, Gleason grading of prostate cancer via MRI/MRS. *Med Image Anal* 17, 219–235.
  - [188] Tiwari, P., Kurhanewicz, J., Rosen, M., Madabhushi, A., 2010. Semi supervised multi kernel (SeSMiK) graph embedding: identifying aggressive prostate cancer via magnetic resonance imaging and spectroscopy. *Med Image Comput Comput Assist Interv* 13, 666–673.
  - [189] Tiwari, P., Madabhushi, A., Rosen, M., 2007. A hierarchical unsupervised spectral clustering scheme for detection of prostate cancer from magnetic resonance spectroscopy (MRS). *Med Image Comput Comput Assist Interv* 10, 278–286.
  - [190] Tiwari, P., Rosen, M., Madabhushi, A., 2008. Consensus-locally linear embedding (C-LLE): application to prostate cancer detection on magnetic resonance spectroscopy. *Med Image Comput Comput Assist Interv* 11, 330–338.
  - [191] Tiwari, P., Rosen, M., Madabhushi, A., 2009a. A hierarchical spectral clustering and nonlinear dimensionality reduction scheme for detection of prostate cancer from magnetic resonance spectroscopy (MRS). *Med Phys* 36, 3927–3939.
  - [192] Tiwari, P., Rosen, M., Reed, G., Kurhanewicz, J., Madabhushi, A., 2009b. Spectral embedding based probabilistic boosting tree (ScEPTre): classifying high dimensional heterogeneous biomedical data. *Med Image Comput Comput Assist Interv* 12, 844–851.
  - [193] Tiwari, P., Viswanath, S., Kurhanewicz, J., Sridhar, A., Madabhushi, A., 2012. Multimodal wavelet embedding representation for data combination (MaWERiC): integrating magnetic resonance imaging and spectroscopy for prostate cancer detection. *NMR Biomed* 25, 607–619.
  - [194] Tofts, P., 2010. T1-weighted DCE imaging concepts: modelling, acquisition and analysis, in: *Magneton Flash*. Siemens.
  - [195] Tofts, P.S., 1997. Modeling tracer kinetics in dynamic Gd-DTPA MR imaging. *J Magn Reson Imaging* 7, 91–101.
  - [196] Toth, R., Chappelow, J., Rosen, M., Pungavkar, S., Kalyanpur, A., Madabhushi, A., 2008. Multi-attribute non-initializing texture reconstruction based active shape model (MANTRA). *Med Image Comput Comput Assist Interv* 11, 653–661.
  - [197] Toth, R., Doyle, S., Pungavkar, S., Kalyanpur, A., Madabhushi, A., 2009. A boosted ensemble scheme for accurate landmark detection for active shape models, in: *SPIE Medical Imaging*, Orlando, FL.
  - [198] Tu, Z., 2005. Probabilistic boosting-tree: learning discriminative models for classification, recognition, and clustering, in: *Computer Vision, 2005. ICCV 2005. Tenth IEEE International Conference on*, pp. 1589–1596 Vol. 2.
  - [199] Turkbey, B., Choyke, P.L., 2012. Multiparametric MRI and prostate cancer diagnosis and risk stratification. *Curr Opin Urol* 22, 310–315.
  - [200] Vanhamme, L., van den Boogaart, A., Van Huffel, S., 1997. Improved method for accurate and efficient quantification of MRS data with use of prior knowledge. *J. Magn. Reson.* 129, 35–45.
  - [201] Vapnik, V., Lerner, A., 1963. Pattern Recognition using Generalized Portrait Method. *Automation and Remote Control* 24.
  - [202] Verma, S., Rajesh, A., Fütterer, J.J., Turkbey, B., Scheenen, T.W., Pang, Y., Choyke, P.L., Kurhanewicz, J., 2010. Prostate MRI and 3D MR spectroscopy: how we do it. *AJR Am J Roentgenol* 194, 1414–1426.
  - [203] Verma, S., Turkbey, B., Muradyan, N., Rajesh, A., Cornud, F., Haider, M.A., Choyke, P.L., Harisinghani, M., 2012. Overview of dynamic contrast-enhanced MRI in prostate cancer diagnosis and management. *AJR Am J Roentgenol* 198, 1277–1288.
  - [204] Vilanova, J.C., Comet, J., Barceló-Vidal, C., Barceló, J., López-Bonet, E., Maroto, A., Arzoz, M., Moreno, À., Areal,

- J., 2009. Peripheral zone prostate cancer in patients with elevated PSA levels and low free-to-total PSA ratio: detection with MR imaging and MR spectroscopy. *Radiology* 253, 135–143.
- [205] Viola, P., Wells, III, W.M., 1997. Alignment by maximization of mutual information. *Int. J. Comput. Vision* 24, 137–154.
- [206] Viswanath, S., Bloch, B.N., Chappelow, J., Patel, P., Rofsky, N., Lenkinski, R., Genega, E., Madabhushi, A., 2011. Enhanced multi-protocol analysis via intelligent supervised embedding (EMPrAvISE): detecting prostate cancer on multiparametric MRI, in: *Proc. SPIE 7963, Medical Imaging 2011: Computer-Aided Diagnosis*.
- [207] Viswanath, S., Bloch, B.N., Genega, E., Rofsky, N., Lenkinski, R., Chappelow, J., Toth, R., Madabhushi, A., 2008a. A comprehensive segmentation, registration, and cancer detection scheme on 3 Tesla in vivo prostate DCE-MRI. *Med Image Comput Comput Assist Interv* 11, 662–669.
- [208] Viswanath, S., Bloch, B.N., Rosen, M., Chappelow, J., Toth, R., Rofsky, N., Lenkinski, R., Genega, E., Kalyanpur, A., Madabhushi, A., 2009. Integrating structural and functional imaging for computer assisted detection of prostate cancer on multi-protocol in vivo 3 Tesla MRI, in: *Society of Photo-Optical Instrumentation Engineers (SPIE) Conference Series*.
- [209] Viswanath, S., Tiwari, P., Rosen, M., Madabhushi, A., 2008b. A meta-classifier for detecting prostate cancer by quantitative integration of *In Vivo* magnetic resonance spectroscopy and magnetic resonance imaging, in: *Medical Imaging 2008: Computer-Aided Diagnosis, SPIE*.
- [210] Viswanath, S.E., Bloch, N.B., Chappelow, J.C., Toth, R., Rofsky, N.M., Genega, E.M., Lenkinski, R.E., Madabhushi, A., 2012. Central gland and peripheral zone prostate tumors have significantly different quantitative imaging signatures on 3 Tesla endorectal, in vivo T2-weighted MR imagery. *J Magn Reson Imaging* 36, 213–224.
- [211] Vos, P.C., Barentsz, J.O., Karssemeijer, N., Huisman, H.J., 2012. Automatic computer-aided detection of prostate cancer based on multiparametric magnetic resonance image analysis. *Phys Med Biol* 57, 1527–1542.
- [212] Vos, P.C., Hambrock, T., Barentsz, J.O., Huisman, H.J., 2008a. Combining T2-weighted with dynamic MR images for computerized classification of prostate lesions, in: *Medical Imaging 2008: Computer-Aided Diagnosis, SPIE*.
- [213] Vos, P.C., Hambrock, T., Barentsz, J.O., Huisman, H.J., 2010. Computer-assisted analysis of peripheral zone prostate lesions using T2-weighted and dynamic contrast enhanced T1-weighted MRI. *Phys Med Biol* 55, 1719–1734.
- [214] Vos, P.C., Hambrock, T., Hulsbergen-van de Kaa, C.A., Futterer, J.J., Barentsz, J.O., Huisman, H.J., 2008b. Computerized analysis of prostate lesions in the peripheral zone using dynamic contrast enhanced MRI. *Med Phys* 35, 888–899.
- [215] Vovk, U., Pernus, F., Likar, B., 2007. A review of methods for correction of intensity inhomogeneity in MRI. *Medical Imaging, IEEE Transactions on* 26, 405–421.
- [216] Walker, P., Crehan, G., Parfait, S., Cochet, A., Maignon, P., Cormier, L., Brunotte, F., 2010. Absolute quantification in 1H MRSI of the prostate at 3T, in: *ISMRM Annual Meeting 2010*.
- [217] Wang, L., Mazaheri, Y., Zhang, J., Ishill, N.M., Kuroiwa, K., Hricak, H., 2008. Assessment of biologic aggressiveness of prostate cancer: correlation of MR signal intensity with Gleason grade after radical prostatectomy. *Radiology* 246, 168–176.
- [218] Wiart, M., Curiel, L., Gelet, A., Lyonnet, D., Chapelon, J.Y., Rouviere, O., 2007. Influence of perfusion on high-intensity focused ultrasound prostate ablation: a first-pass MRI study. *Magn Reson Med* 58, 119–127.
- [219] Ye, L., Kynaston, H.G., Jiang, W.G., 2007. Bone metastasis in prostate cancer: molecular and cellular mechanisms (Review). *Int. J. Mol. Med* 20, 103–111.
- [220] Zelhof, B., Lowry, M., Rodrigues, G., Kraus, S., Turnbull, L., 2009. Description of magnetic resonance imaging-derived enhancement variables in pathologically confirmed prostate cancer and normal peripheral zone regions. *BJU Int.* 104, 621–627.
- [221] Zhao, G., Ahonen, T., Matas, J., Pietikainen, M., 2012. Rotation-Invariant Image and Video Description With Local Binary Pattern Features. *Image Processing, IEEE Transactions on* 21, 1465–1477.
- [222] Zhu, H., Ouwerkerk, R., Barker, P.B., 2010. Dual-band water and lipid suppression for MR spectroscopic imaging at 3

- Tesla. *Magn Reson Med* 63, 1486–1492.
- [223] Zitová, B., Flusser, J., 2003. Image registration methods: a survey. *Image and Vision Computing* 21, 977 – 1000.